

Les Trente Glorieuses: 29 years of helioseismic observations with the Luminosity Oscillations Imager

T. Appourchaux^{*} 

Institut d'Astrophysique Spatiale, UMR8617, Université Paris-Saclay, 91405 Orsay Cedex, France

Received 20 September 2025 / Accepted 13 November 2025

ABSTRACT

Context. The Luminosity Oscillations Imager (LOI) of the Variability of Solar Irradiance and Gravity Oscillations (VIRGO) instrument on board the SoHO mission has been operating for almost 30 years.

Aims. The goal of this article is to report on the observation of p -mode parameters throughout these 30 years, which cover two solar cycles, using the LOI scientific and guiding pixels as well as the guiding high-voltage housekeeping. The article also provides a definitive description of the data for the final SoHO archive. The LOI time series analysed here starts on 1 April 1996 0:00 TAI and ends on 31 March 2025 23:59 TAI with a 60 s cadence.

Methods. I use the level 0 data of the LOI to compute level 2 corrected time series for each pixel taking into account engineering calibration, the presence of attractors (locked values), and the SoHO-Sun distance, the spacecraft roll. I used the scientific pixels to derive Sun-as-a-star signals, individual (l, m) signals, east-west and north-south difference signals, guiding pixel signals and east-west and north-south high-voltage signals to compute 29 one-year power spectra. A 29-year time series of the Sun-as-a-star signal was also used to push the detection of p modes to low frequency. The power spectra were globally fitted (fully over the p -mode envelope) using maximum likelihood estimators using a C++ code with two versions of the code depending on the presence of $l = 0$ modes (progFIT and guiFIT). The Fourier spectra for the individual (l, m) signals are locally fitted (around each p -mode) using maximum likelihood estimators using an IDL code for $l \leq 3$.

Results. I report on the effect of solar activity upon mode frequencies, linewidths, heights, and energy rates. I report on the variation as a function of frequency for frequency, a_2 coefficient and linewidth changes, as well as the average over the degree and the frequency of these changes. Using the 29-year time series, I report on the frequencies, linewidths and mode heights fitted with progFIT. Using the collapsogram technique, I also report on the detection of modes below 1600 μ Hz, making the lowest frequencies detected with an instrument observing the Sun in intensity. I also report on the detection of p modes in the high-voltage and guiding pixel signals with a mode height about five to ten times larger than is observed in the Sun-as-a-star signal for $l = 1$. The ratios of the observed mode visibilities for the different signals are provided following a calibration of the size of the guiding pixels. While the visibility ratios for the signals excluding the limb are in good agreement with theory, those covering the solar limb are in strong disagreement.

Key words. methods: numerical – space vehicles: instruments – Sun: helioseismology

1. Introduction

Helioseismology started in the late 1970s with the first detection of global solar p modes by Claverie et al. (1979), later confirmed by Grec et al. (1980) using radial velocity measurements and by Woodard & Hudson (1983) using irradiance measurements with the ACRIM Monitor (Active Cavity Radiometer Irradiance, Willson 1979) on board the Solar Maximum Mission (SMM). These breakthroughs were followed by the first inversion of the solar structure performed by Gough (1984) and Duvall et al. (1984) using the Duvall's law (Duvall & Harvey 1984). Helioseismology became a very useful tool when it demonstrated that the equation of state could be in error, and was indeed in error (Kosovichev et al. 1992).

The diagnostic potential of helioseismology for our physics had already been perceived in the mid-1980s when the Solar and Heliospheric Observatory (SoHO), an ESA/NASA space mission (Special volumes of *Solar Physics*, 1995, vol. 162; 1997, vol. 170; and 1997, vol. 175) was approved. The need for uninterrupted data can be fulfilled by a space mission, but also by

ground-based networks of instrument, networks on which the Sun never sets: the Global Oscillation Network Group (GONG) (dedicated volume of *Science*, 1996, vol. 272), the Investigation on the Rotation and Interior of the Sun (IRIS, Fossat 1991) and the Birmingham Solar-Oscillations Network (BiSON, Elsworth et al. 1991).

The detection of solar oscillations using solar radial velocities is feasible from the ground. It is not so obvious how to perform such measurements using irradiance or radiance fluctuations because of transmission variations through the Earth's atmosphere. Following the detection of p modes with the ACRIM instrument, Fröhlich & Van der Raay (1984) used photometers on board balloons to reduce the impact of the Earth's atmosphere on the measurements. A similar photometer (IPHIR: InterPlanetary Helioseismology by IRradiance measurements, Fröhlich et al. 1988) was flown on board PHOBOS II (Soviet Mars exploration mission, see Siddiqi 2016). This instrument returned excellent helioseismic measurements as shown by Toutain & Fröhlich (1992).

In 1987, the SoHO mission was selected by the European Space Agency as part of its Horizon 2000 programme. The mission consisted of in situ, coronal, particle, and

* Corresponding author: Thierry.Appourchaux@cnr.fr

helioseismic instruments. Following the recent developments in helioseismology (recent at that times), three helioseismic instruments were included for obtaining solar radial-velocity and irradiance measurements using either imagers or looking at the Sun as a star. The Global Oscillations at Low Frequency (GOLF, Gabriel et al. 1995) uses a sodium cell to measure solar radial velocities while looking at the Sun as a star, while the Michelson Doppler Imager (MDI, Scherrer et al. 1995) uses a one-million pixel detector to obtain spatially resolved data. The Variability of IRradiance and Gravity Oscillations (VIRGO, Fröhlich et al. 1995) instrument measures the irradiance of the Sun as a star, the spectral radiance with photometers, and the spectral radiance spatially resolved over the solar disk. The last is performed by the Luminosity Oscillations Imager (LOI) whose concept was described by Andersen et al. (1988), and later built as a space instrument (Appourchaux et al. 1997).

The LOI is one of a kind; it is the only instrument that detected in intensity the low-degree p modes from the ground (Appourchaux et al. 1995), and that has been measuring the low-degree p modes from space since 1996. Its design was specifically aimed at detecting modes with a different sensitivity for degree greater than 1, thereby optimizing the chance of detecting the solar g modes using different signals. Instruments that detect p modes in velocity, such as GOLF and BiSON (Broomhall et al. 2007) or the Helioseismic and Magnetic Imager (HMI, Scherrer et al. 2012) and GONG (Appourchaux 2024), benefit from a better signal-to-noise ratio that allows them to detect modes below $1000 \mu\text{Hz}$. In addition, instruments such as GONG, MDI, and HMI make images of the Sun which permits them to derive by inversion the internal structure from the surface below the convection zone. Nevertheless, it must be emphasized that scientific progress should not always be ranked by the ability of making interesting discoveries, but also by the ability of confirming new discoveries. The failure to confirm g -mode detection can serve as an example (Appourchaux et al. 2000, 2010).

The LOI is not merely another helioseismic instrument; it can contribute to the understanding of several sources of systematic errors. For instance, it was demonstrated by Toutain et al. (1997) that observations of solar p modes in intensity indeed look different from those performed in velocity. This resulted in the discovery of p -mode profile asymmetries (Toutain et al. 1998). It was also shown by Schou et al. (2002) that rotation inversions are very sensitive to different frequency inferences made with different instruments. Last but not least, the LOI has a different mode sensitivity as it observes in intensity; the mode leakage is therefore significantly different from that of velocity instruments, as are the systematic errors associated with this leakage.

The goals of this article are 1) to explain how the time series of the LOI pixels are constructed, and to provide this information to the solar community; 2) to show that an instrument detecting solar p modes in intensity confirms most of the discovery performed in velocity; and 3) to report on the limb amplification of the p modes. The LOI time series analysed here starts on 1 April 1996 0:00 TAI and ends on 31 March 2025 23:59 TAI with a 60 s cadence.

Section 2 of the article describes the data reduction, and production of level 1 data. Section 3 explains which times series were computed. Section 4 explains how the resulting power spectra were fitted for p -mode parameter extraction. The following sections provide results of the variations of the p -mode parameters over two solar cycles, the impact of gaps, the frequency error bars, the mode amplitude and height. The last

section gives results from the various guiding signals before concluding.

2. From level 0 to level 1: Calibration

The design of the LOI instrument is described in Appourchaux et al. (1997). The data reduction has been heavily modified since then. Especially, the occurrence of locked value on the pixel data, known as attractors, requires a special treatment for identifying them and flagging them. The attractors are values that are locked at some binary values, locking that is most likely occurring in the Voltage-to-Frequency converters used for the Analog to Digital conversion in the VIRGO instrument. The Sunphotometers (SPM) of VIRGO are also affected by this locking. Other corrections related to the loss of the pointing of the High Gain Antenna (HGA) are also required. All these steps are described hereafter.

2.1. Level 0: Depacketization

After depacketizing of the transmitted data, the level 0 data were built from the three transmissions of the VIRGO data; this was done at the VIRGO Data Centre (VDC) located at the Instituto de Astrofísica de Canarias, Tenerife, Spain. Preliminary detection of the attractors was done at the VDC but I used my own algorithm described hereafter for flagging them.

2.2. Level 0: Attractor detection and flagging

The attractors are best detected in the raw binary data before conversion to engineering values. The detection was performed day by day, pixel by pixel. The procedure is as follows:

- First, detect if there were any jumps greater than 0.4% of the median in consecutive data points
- Second, if no jumps were detected proceed with the next step, otherwise no attractor detection performed.
- Third, I computed the mean and the rms of the data. I arbitrarily limited the detection of the attractors to values within $\pm 4\sigma$ of the mean.
- Third, I computed the histogram of the data using a bin size of 1% of the data variation (maximum-minimum)
- Fourth, the histogram was binned with a box car over 30 bins (with edge mirrored)
- Fifth, I computed the ratio of the histogram to that of the binned histogram.
- Sixth, the attractors were then detected when the ratio is greater than $5.6\sigma_s$, where the σ_s is the estimated value of the rms ratio for the associated bin value (shot noise). The attractor values were then replaced by a value of -10 .

The procedure works in nearly all circumstances. Given the fact, that this procedure was applied daily more than 120 000 times in total in the course of 29 years, there were still circumstances that would make this procedure fails. For instance, when there was a sunspot appearing on a pixel there is a large variation of several % that would distort the histogram. In order to reduce, the over-detection or under-detection, I decided to conduct a visual check of the detected attractors, especially when the daily variations were larger than some predetermined value ($>0.3\%$) typical of a small sunspot crossing a pixel.

Figure 1 gives an example of attractor detection. It shows the first detected attractor. The occurrence of these attractors does not depend upon the pixels but on the digital value itself. Since

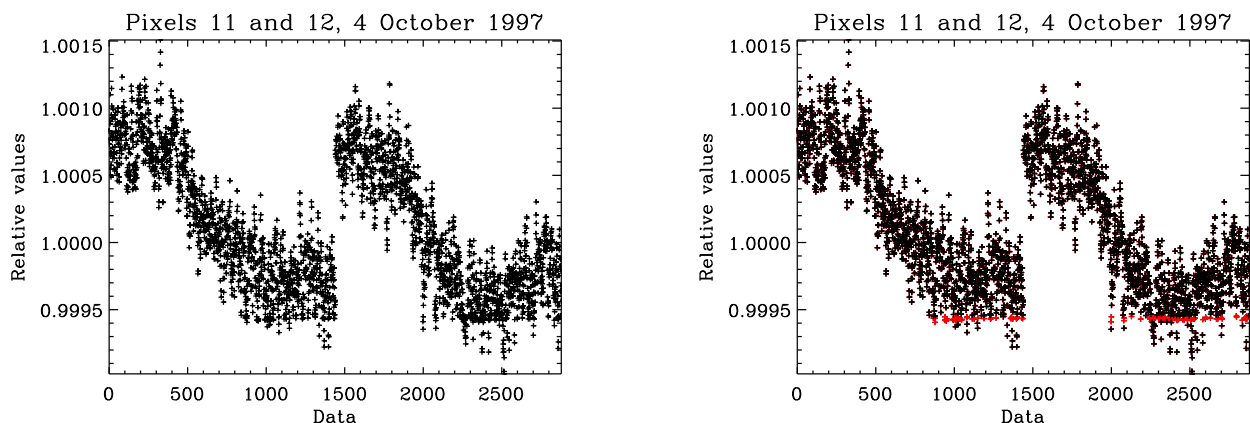


Fig. 1. Relative pixel intensity as a function of time in minutes for two pixels: raw (left), identified attractors in red (right).

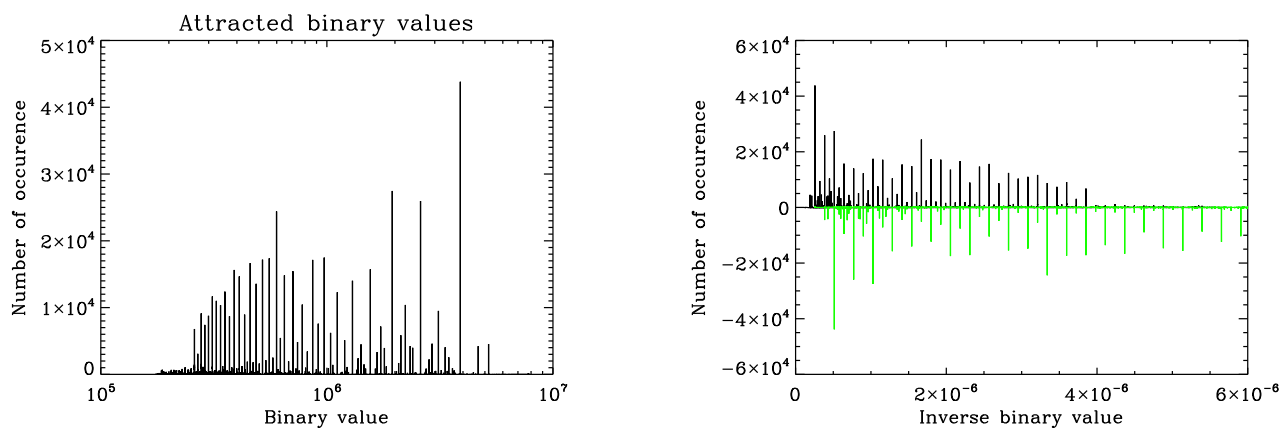


Fig. 2. Compilation of all attracted bits over the 12 scientific pixels over 29 years as a function of the binary value (left) and as a function of the inverse binary value (right). For the latter in addition, shown in green and mirrored the same compilation but as a function the inverse binary value multiplied by a factor of 2.

the instrument has a decreasing throughput of about a factor of 16 in 29 years, when the pixels with the smallest flux (Pixels 9–12) have an attractor, the other pixels with larger surface will also have the attractor at the same value at a later time. Figure 2 gives an histogram of all of the digital values corresponding to attractors. There is a clear periodicity in the inverse of the binary value shown by Fig. 2. The periodicity corresponds to a ratio between the inverse binary value of about a factor of 1.0625, which exactly corresponds to a multiplication by $1 + 1/16$. In binary calculation, this multiplication corresponds to adding the original binary value (1) to the binary value shifted down by four bits ($1/16$). The fact that there is also a correspondence with a factor of two which is a binary value shifted down one bit may give clues to the source of the attractors. There are also counters behind the VFC that can count up to 24 bits. It is possible that the locking occurs not in the VFC but more likely in the counters themselves.

The flag of the attractors are kept until the outliers are cleaned (see Section 3.2). At most, there are no more than six attractors at any one time, thereby affecting half of the LOI pixels. The impact of the attractors on the data is studied in Section 3.2.

2.3. Level 1: Engineering data conversion

The level 0 data are then calibrated to engineering units using the calibration performed on the ground before launch. The calibration of the offset for each pixel was refined in flight with the calibration-mode switch off. The data are then corrected for temperature effects and pixel-sensitivity variations.

2.4. Level 1: Sun distance and spacecraft attitude corrections

The 16 pixels were then converted to flux measured at 1 AU using the SoHO-Sun distance derived from the orbital data (See Appourchaux et al. 1997, for the configuration of the pixels on the detector). The correction took into account the real shape of the pixels, the limb darkening at 500 nm, and the in-flight size of the solar image at 1 AU. The precision of the correction is better than 0.1% for all of the scientific pixels. In addition a relativistic correction was applied taking into account the spacecraft velocity with respect to the Sun; this is minute. All of these corrections were described in the LOI VDC document available on the VIRGO home page under www.ias.u-psud.fr/virgo/html/software.html. In addition, for

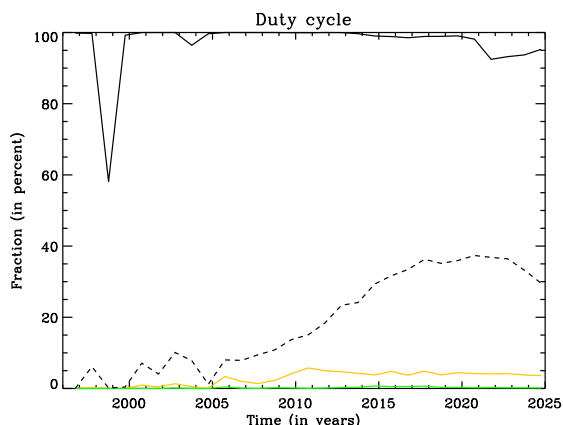


Fig. 3. Duty cycle as a function of time for the 12-pixel data (continuous line), for the fraction of time any pixel having at least one attractor (dashed line), for the fraction of time at least one pixel having an attractor lasting longer than 5 minutes (orange line), and for the fraction of time at least two pixels having an attractor lasting longer than five minutes (green lines).

taking into account the pixel response that depends on the spacecraft (S/C) attitude, I used the sensitivities derived by Appourchaux et al. (1997) for correcting for the impact of the varying angle of incidence of the sunlight on the LOI instrument.

3. From level 1 to level 2

3.1. Roll maneuver correction

After May 25, 2003, the HGA failed to move for sending data towards the Earth. It was then decided to leave the HGA in a fixed position and rotate the spacecraft by 180 degrees every 3 months for transmitting to Earth¹. When the S/C is rolled by 180 degrees, the pixel numbering is redefined in the process, i.e. pixels 1, 2, 5, 6, 7, 8 becoming pixels 4, 3, 8, 7, 6, 5 and vice versa; and the guiding pixels 13, 14 becoming 16, 15 and vice versa.

During the roll maneuvers, the rotation was not done exactly around the line of sight of the instrument requiring an adjustment the pointing of the instrument. In the process, this slight de-pointing produced a slight change in the flux measured by each pixel. The impact of the roll was to slightly change the pixel response. The correction of these changes were done for each pixel, as

- First, get date and time of the roll by using the S/C attitude data
- Second, the pixel flux was fitted over one day ending 200 minutes before the roll, and starting 200 minutes after the roll.
- Third, the flux before and after the roll were then extrapolated for each fit at the time of the roll.
- Fourth, the correction was done by normalizing the flux after the roll to that of the flux before the roll.

This normalization makes sure that the time series is homogeneous since the start of the mission.

¹ See https://soho.nascom.nasa.gov/soc/soho_events/SOHO-Spacecraft-Events.csv

3.2. Outlier cleaning

The various interruptions due either to the extended loss of contact (known as the SoHO vacations, mid-1998), the roll maneuvers, the presence of attractors or other unforeseen events produce large jumps in the pixel data that need to be corrected for. I used an automatic outlier detection based upon the Peirce criterion (Peirce 1852; Gould 1855). The correction for each pixel is done as

- First, detect outliers with the Peirce criterion over a duration of 10 days. The detection and correction were done automatically. The detected outliers were filled by interpolation.
- Second, detect outliers with the Peirce criterion over a duration of 360 days. The detection can be done either automatically (default) or interactively (choice of the user). If the correction was done interactively, the user chooses two locations over which to perform the interpolation. The latter was used when very large jumps cannot be corrected automatically. This step was done recursively until no correction is necessary.
- Third, detect outliers with the Peirce criterion over a duration of 40 days with the same procedure as for the previous step.

During this process, the attractors are detected as outliers and corrected by interpolation, thereby filling the gaps created by these attractors. Figure 3 shows the impact of the attractors on the duty cycle of the data. At the end of the mission, the data have attractors about 40% of the time. The increase of the number of attractors is mainly due to the fact that the photon flux on the pixels decreased by factor of 16 over the 29 years, hence the change in digital count is smaller at the end of the 29 years compared to the beginning, making the attractors lasting longer at the end than at the beginning. But since the attractors are not always continuous, the interpolation can easily fill them in when they are shorter than five minutes. The number of pixels having an attractor lasting more than five minutes is at most 5%, while it is less than 0.5% for two attractors.

3.3. Detrending and filtering of pixel data

For each pixel, the data were detrended using a triangular two-day smoothing window. The relative values were then computed and all spikes greater than 30σ are removed. Since the 12 pixels may have some missing value (set to zero), a further filtering is done by setting all pixels to zero if at least one pixel is missing in all the three quadruplets: Pixel 1–4, Pixel 4–8, and Pixel 9–12. The 12 pixels are then not set to zero if for any datum at most two pixel quadruplets have missing data. The time series analysed of all 16 pixels are available from soho.nascom.nasa.gov/data/archive.html.

4. Generation of time series

4.1. Sun-as-a-star time series

The dataset for the Sun-as-a-star time series or Full-disk (FD) time series was derived from the average of the 12 level 2 scientific pixels. The time series were made of two sets: one time series of 29 years duration, 29 time series of one-year duration. Examples for the power spectra for the first year and the last year are shown on Figure 4. The power spectra were corrected by dividing by the duty cycle (see Figure 3).

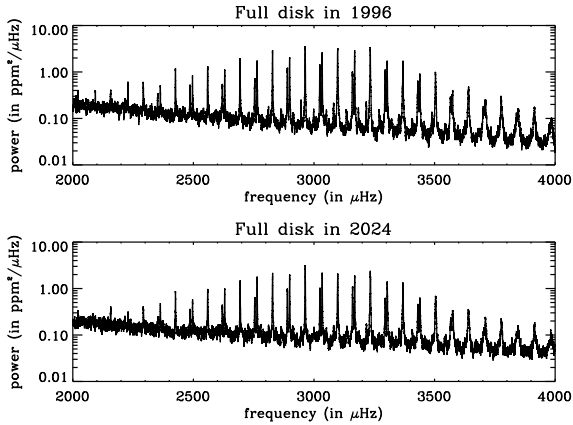


Fig. 4. Power spectrum as a function of frequency for the full disk signal for 1996 (top) and 2024 (bottom) for one year of data.

4.2. Spherical harmonics extraction

For combining the pixel data, I used the spherical harmonic decomposition computed as in Appourchaux & Andersen (1990), using the limb darkening from Allen (1975). The filters were normalized according to Eq. (17) of Appourchaux et al. (1998a). This normalization allows a symmetrical leakage matrix (Appourchaux et al. 1998a). Example for such leakage matrix can be found in Appourchaux et al. (1998c). Since the apparent solar diameter changes along the orbit, the spherical harmonic filters vary slowly with time. To alleviate this problem, time-independent filters were applied to the pixels to extract the (l, m) modes. The filters were computed as an average over one year of filters computed weekly. Over this period the B angle has a mean close to zero. Gizon et al. (1998) showed that it was possible to detect the influence of a non-zero B angle on the p -mode data. Therefore, this average minimizes the effect of the B angle on the data. After combining the pixels with the filters, the time series are Fourier transformed; the positive frequencies provide the signal for $+m$, and the negative frequencies provide the conjugate of the signal for $-m$ (Appourchaux et al. 1998a).

For each (l, m) harmonic, I extracted two datasets: one time series of 29 years duration and 29 time series of one-year duration.

4.3. East-west and north-south time series

I also extracted the difference between the north-south (NS) pixels and the east-west (EW) pixels. For the NS pixels, this is simply the same dataset as for $l = 1, m = 0$. For the EW pixels, this is the difference between the $l = 1, m = 1$ complex time series and its conjugate. For each, I extracted 29 time series of one year duration. These datasets were used to compare the result obtained with the high-voltage (HV) signals, which are sensitive to the difference between the north and south guiding pixels and between the east and west guiding pixels.

4.4. EW – NS HV and guiding pixel time series

I also extracted from the engineering data, the high-voltage time series for the Y direction (north-south) and the Z direction (east-west). The voltages were converted to arcsec then to ppm. The value of 8.8 ppm/marcsec is derived from the outer radius of the

scientific pixels given above and from the calibration performed in April 1996 (Appourchaux et al. 1997). Figure 5 shows two power spectra at the beginning of the mission and near the end of the mission. The improvement in signal-to-noise ratio is striking but is not understood. On the other hand, the guiding pixels also show the p modes but only for the first year (1996) (Figure 6) since the noise increases by such a factor that no modes can be detected after 1997, which is not understood either. Similar power spectra were derived with six months of data by Appourchaux & Toutain (1998).

5. p -mode parameter extraction

They are 30 Sun-as-a-star power spectra, 29 north-south difference power spectra, 29 east-west difference power spectra, two guiding pixel power spectra, 29 north-south high-voltage power spectra, 29 east-west high-voltage power spectra, and 29×15 (l, m) power spectra.

5.1. Power spectra fitting

The power spectra were fitted using maximum likelihood estimators (MLE) (Schou 1992; Appourchaux et al. 1998a). The power spectra were fitted globally (fully over the p -mode envelope), an approach first used for fitting stellar power spectra as in Appourchaux et al. (2008). In that latter article, the MLE for HD49933 was made difficult due to the large linewidth of the modes making the identification of the pair $l = 0-2$ with respect to the $l = 1$ difficult. It was already suggested by Appourchaux et al. (2008) that a Bayesian approach would be better providing a more conservative identification of the modes; such an approach was implemented by Benomar et al. (2009). This Bayesian approach that I suggested is now widely used in asteroseismology (Handberg & Campante 2011; Corsaro & De Ridder 2014; Lund et al. 2017). The Bayesian fit of the power spectra is remarkably efficient when the S/N ratio in the power spectrum is low, less than about 3, but when the signal ratio is higher the MLE fit and the Bayesian fit provide to the same estimators with very similar error bars. In addition, the Bayesian fit requires the creation of Markov Chains Monte Carlo estimates which can be very slow in any interpreted language (Python, IDL).

The code used by Appourchaux et al. (2008) for the CoRoT star HD49933 was indeed an IDL code. There were already attempts to write a C++ code (progFIT) based on this IDL code (Neiner & Appourchaux 2004) which was not yet available in 2008. The development of that code continued until 2010, but the code was not still fully functioning (Neiner, private communication). The code was then picked up from its ashes in 2021 when its use for the Planetary transits and oscillations of stars (PLATO) mission was considered an asset given the large sample of solar-like stars (About more than 20 000 stars for the core P1 sample, Rauer et al. 2025). The code was then made fully functional and was tested for the PLATO mission on hundreds of solar-like stars. The code can be found on Gitlab². The specificity of progFIT is that it uses the Munit2 library for finding the highest likelihood, but it not only finds the highest likelihood (or log(likelihood) minimum) it also check that the distance between the minimum found and the extrapolated minimum is small compared to a given criteria, i.e. providing the estimated distance to minimum (EDM). The Hessian (used for getting the

² git.ias.u-psud.fr/plato_pdc/plato_wp37/wp372_msap3/msap3_04/progfit

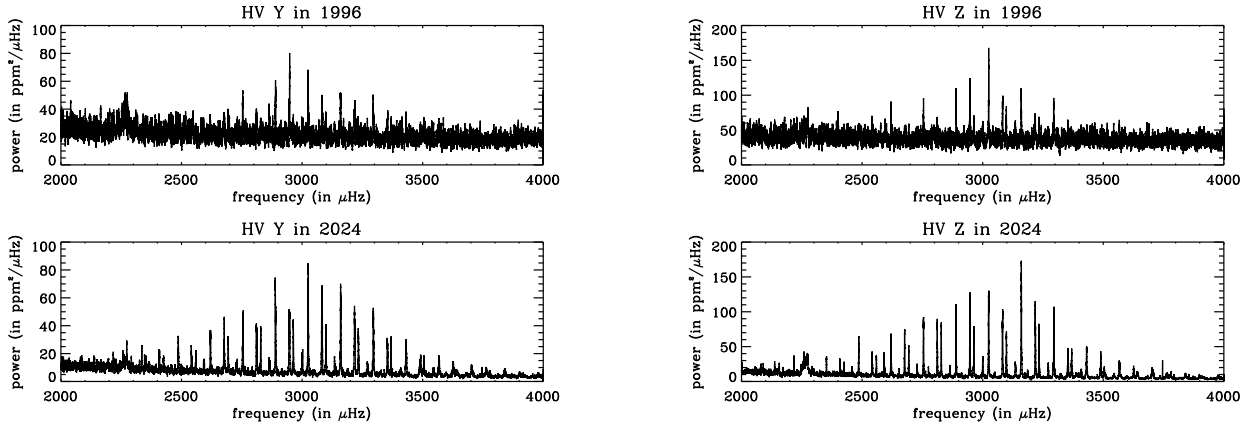


Fig. 5. (left) Power spectrum as a function of frequency for the *Y* high-voltage for 1996 (top) and 2024 (bottom) for one year of data. (right) Power spectrum as a function of frequency for the *Z* high-voltage for 1996 (top) and 2024 (bottom) for one year of data.

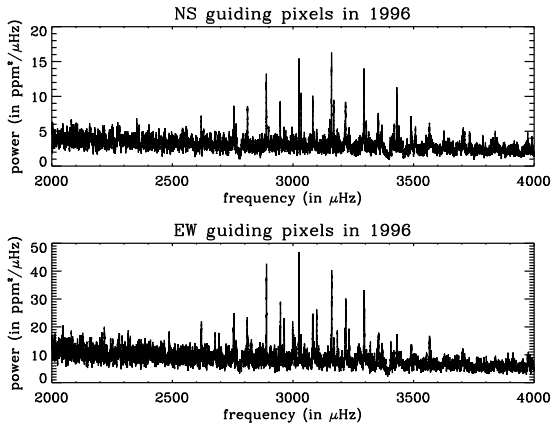


Fig. 6. Power spectrum as a function of frequency for 1996, for the north-south (NS) guiding pixels (top) and for the east-west (EW) guiding pixels (bottom) for one year of data.

parameter errors) is computed on the fly as well as the EDM. The EDM is a representation that in the found minimum is within a typical σ distance in the hypersphere of the N parameters modelling the power spectrum. The EDM is a dimensionless quantity that can be written as

$$\text{EDM} = \frac{1}{2} \sum_{i=1}^{i=N} (d_i^r)^2 = \frac{N}{2} \langle d^r \rangle^2 \quad (1)$$

where d_i^r is the relative distance to minimum in units of σ_i , and $\langle d^r \rangle$ is the mean relative distance over the N parameters. For 200 parameters and a mean $\langle d^r \rangle$ of 3%, the resulting EDM is 0.1. I used this latter value for the convergence of all fits. For an EDM of 0.1, when the number of parameters is decreased to 100, the mean distance to the minimum increases by a factor of $\sqrt{2}$, still sufficient for most applications.

For `progFIT`, the typical speed is 22 minutes on an Apple M3 Max, for a one-year duration time series, with 19 quadruplets $l = 0, 1, 2$ and 3 for a total of 166 parameters: 10 parameters for the background (three Harvey-like profiles with exponent of 4 and one white noise), one common splitting for all

degrees, one common inclination angle for all degrees, one common ratio between the heights of the $l = 2$ modes to $l = 0$ modes, one common ratio between the heights of the $l = 3$ modes to $l = 1$ modes and 8 parameters per quadruplet (four frequencies, two linewidths (one for the $l = 0-2$ pair and one for the $l = 1-3$ pair), two mode heights) assuming a symmetrical Lorentzian profile; the ratio within a multiplet follows [Toutain & Gouttebroze \(1993\)](#). For the 29-year duration time series, it takes 8 hours with 23 quadruplets.

Following the successful development of `progFIT`, another code was developed for fitting the NS and EW difference signals, and HV guiding signals. Since these signals are by construction not sensitive to $l = 0$ modes, the new code (`guiFIT`) took into account this lack of visibility, but also the different visibilities in a multiplet. The code can also be found on [Gitlab³](#).

The `progFIT` code was used 62 times on the FD and guiding pixel power spectra, while `guiFIT` was used 116 times. In total, the two codes were used less than about 180 times resulting in a bit less of 3 days of computing on a single processor, in comparison the former IDL code would have taken about 150 days of computing. With several cores such as the M3 Max, the duration reduces even further to about five hours.

5.2. Fourier spectrum fitting

This technique, known as phase fit, was introduced by [Schou \(1992\)](#) and later refined by [Appourchaux et al. \(1998a\)](#). The method relies on the knowledge of the leakage matrix for inferring the p -mode parameters. This method can only be applied when the leakage matrix for a given degree can be inverted ([Appourchaux et al. 1998a](#)).

The p -mode parameters were usually locally extracted (around each p -mode) from the Fourier spectra using MLE ([Schou 1992](#); [Appourchaux et al. 1998a](#)) with an IDL code. The splittings were derived from Clebsh-Gordan coefficients as in [Ritzwoller & Lively \(1991\)](#), the decomposition is given in [Appendix A](#). Three pixel noises were used for modelling the solar noise, while the leakage and noise covariance matrix were derived according to [Appourchaux et al. \(1998a\)](#). Exam-

³ git.ias.u-psud.fr/plato_pdc/plato_wp37/wp372_msap3/msap3_04/guifit

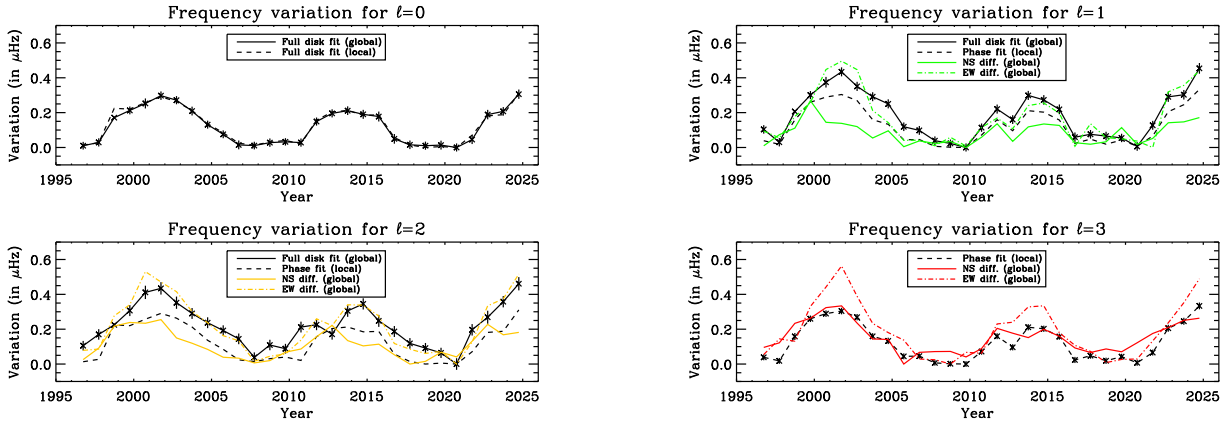


Fig. 7. Mean mode frequency variation as a function of time. (Top, left) for the $l = 0$ modes for the global fit (continuous line) and the local fit (dashed line). (Top, right) for the $l = 1$ modes for the global fit (continuous line), the local phase fit (dashed line), the global fit of north-south difference (green line) and the global fit of east-west difference (green dashed line). (Bottom, left) for the $l = 2$ modes for the global fit (continuous line), the local phase fit (dashed line), the global fit of north-south difference (orange line) and the global fit of east-west difference (orange dashed line). (Bottom, right) for the $l = 3$ modes for the local phase fit (dashed line), the global fit of north-south difference (red line) and the global fit of east-west difference (red dashed line). The $l = 3$ modes are not shown because they are too faint to give a meaningful full-disk signals.

ples of Fourier spectra for various l and m can be found in Appourchaux et al. (1998c).

Here I do not study the odd a -coefficients that are related to the solar differential rotation. Although results on these coefficients are available with the LOI (Appourchaux et al. 1998b) their use has to be combined with higher degree modes for getting a proper rotation inversion (See Appourchaux et al. 2002). Since the LOI does not provide high degree modes, work using the GONG and HMI/MDI data provides odd a -coefficients covering all degrees from 0 to 200 with a single instrument (Korzennik 2023) allowing homogenous rotation inversion.

6. p -mode parameters as a function of solar activity

The dependence of the p -mode parameters upon solar activity was studied against the flux at 10.7 cm. This flux is the manifestation of the existence of magnetic fields on the surface of the Sun.

The 10.7 cm flux could be downloaded at the SIDC (Solar Influence Data Analysis Center) in 2023 with a time series running from April 1, 1996 to March 31, 2021; the data are at the time of writing no longer available. The flux can now be found daily thanks to Space Weather Canada⁴, and the two time series were merged into a single time series from April 1, 1996 to March 31, 2025, to produce a yearly average. Since I used the 29 yearly time series of the different signals for that study, I also averaged the flux over the same period of one year. The 29 power spectra were fitted using a variable and a fixed noise background. The two fits were used to reduce the bias on linewidths and mode heights that occurs when one uses a different background (See for instance Appourchaux et al. 2014).

6.1. Frequencies

The impact of solar activity on the frequency and the various even a -coefficients of the splitting was first studied by Libbrecht & Woodard (1990). The even coefficients are directly

⁴ spaceweather.gc.ca/forecast-previous/solar-solaire/solarflux/sx-5-en.php

related to the decomposition of the magnetic field perturbation on even-order Legendre polynomials (Antia et al. 2001).

For studying the frequency variation over the solar cycle, I used Eq. (5) of Chaplin et al. (2004) that includes a correction for the mode inertia and a function $\mathcal{F}(\nu)$ that measures the variation of the frequency shift over frequency, normalized to 1 at 3 μHz . This latter function was fitted from Figure 1 of Chaplin et al. (2004) as

$$\mathcal{F}(\nu) = 1.678 - 6.794(\nu_{3000}) + 7.784(\nu_{3000})^2 - 1.669(\nu_{3000})^3 \quad (2)$$

where (ν_{3000}) is the frequency normalized to 3000 μHz . The weighting as provided by their Eq. (5) is a way to relate all frequency variations to a single frequency of 3000 μHz , then $\mathcal{F}(\nu)$ can provide the frequency shift at any given frequency if needed. The weighting scheme is used over the frequency range from 2400 μHz to 3500 μHz for obtaining the variations for each degree, and over all degrees up to $l = 3$.

6.1.1. Dependence on the degree and frequency

Figure 7 shows the frequency shift for $l = 0, 1, 2$ and 3, either fitted globally for the Sun-as-a-star signal and the difference signals of the resolved image (EW and NS) or locally with the resolved image. The maximum frequency variation is typically 0.3 to 0.4 μHz , depending on the degree. For the $l = 0$ mode, there is no difference between the local and the global fit. For the other degrees, there are differences due to the impact of the a_2 - and a_4 -coefficients upon the frequency shift. For l different from 0, each signal has a different dependence upon the a_2 - and a_4 -coefficients. The frequency shift for each signal depends upon the visibility of each (l, m) component. For the NS differences and the HV Z, the signals are primarily sensitive to the $m = 0$ modes for $l \leq 2$. For the EW differences and the HV Y, the signals are primarily sensitive to the $m = \pm l$ modes for $l \leq 2$. For the FD signals, the sensitivity varies with the degree for which the dependence of the measured frequency was given by Appourchaux & Chaplin (2007). Table 1 gives the frequency dependence for all these signals and degrees. Figure 7 clearly shows the result of Table 1.

Table 1. Frequency as a function of the degree and the signals. ν_l^{res} is the frequency obtained using the phase fit of the resolved data. For the FD signal and $l = 2$, the dependence is derived from Appourchaux et al. (2007) for a linewidth of 1 μHz .

Signal	$l = 0$	$l = 1$	$l = 2$
EW/HV Y	–	$\nu_1^{\text{res}} + a_2$	$\nu_2^{\text{res}} + 2a_2 + 2a_4$
Full disk	ν_0^{res}	$\nu_1^{\text{res}} + a_2$	$\nu_2^{\text{res}} + 1.6a_2 + 3a_4$
NS/HV Z	–	$\nu_1^{\text{res}} - 2a_2$	$\nu_2^{\text{res}} - a_2 - 8a_4$

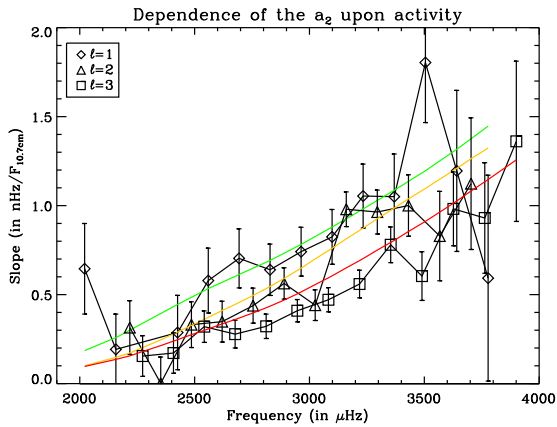


Fig. 8. Slope of the dependence of the a_2 -coefficient to the 10.7 cm flux as a function of frequency for degrees $l = 1, 2$ and 3 . A second-order polynomial fit is shown for each degree: $l = 1$ (green line), $l = 2$ (orange line), and $l = 3$ (red line). The data used were the resolved data locally fitted.

Using the resolved data, I derived the dependence of the a_2 -coefficient upon the 10.7 cm flux for the three different degrees. Figure 8 shows the slope of the linear fit of a_2 to the 10.7 cm flux. Over the 29 years, the maximum variation of the a_2 -coefficient is about 0.1 μHz (with the impact of the a_4 being negligible) resulting in a difference between the EW- and NS-signal frequency shift of about 0.3 μHz at the maximum of activity (see Fig. 7 and Table 1).

6.1.2. Degree and frequency averaging

The averaging done over the frequency range can also be combined for averaging over the degrees. Figure 9 shows the averaged frequency shift over various degrees for the FD signals, the NS signals (difference and HV Z) and the EW signals (difference and HV Y). It is clear that the difference in frequency shift is due to the different mode sensitivity whose variation with m results in a different sensitivity to the solar activity belt. In addition, the variations are the same for the NS/EW differences and the HV Z/HV Y signals (see Table 1).

The averaging over frequency and degree can also be done using a time-travel technique (Vasilyev & Gizon 2024). Although their claims of being a simpler method than mode frequency fitting is matter of debate, they still find similar variations with solar activity for the mean mode time travel.

6.1.3. Frequency error bars

I also compared the formal error bars obtained with the global MLE estimation with that of the rms deviation of the individual frequencies. Since the frequencies vary with the solar activity, I compensated the variations for each degree and the solar-activity level as given by the 10.7 cm flux. After subtraction of the frequency shift which increases with frequency until 4000 μHz (see Figure 10), I was able to infer the rms variations for each degree and frequency. Figure 11 gives the rms and formal errors for each degree for the FD signal, while Figure 12 gives the ratio of the rms errors to the formal errors for $l = 0-3$. The formal errors are typically smaller by 20–30% smaller than the rms errors. Such underestimation was also measured for the 45-year of BiSON splittings (Howe et al. 2023). This underestimation does not contradict the fact that the MLE errors are bounded on the low side by the Cramer-Rao theorem (Appourchaux et al. 1998a). The same bounding occurs with a Bayesian fit since in that case one must use the Van Trees (Van Trees 1968) inequality taking also into account the information prior. The two inequalities are such that the Bayesian bound is lower than the classical MLE bound (See also Echeverria et al. 2016, for a hands-on application). When there is no information, the two bounds are identical.

6.2. Linewidth and mode heights

The variation of low degree mode linewidths and mode heights were reported by Chaplin et al. (2000) using BiSON data. Similar variations were found by Jiménez-Reyes et al. (2003) for GOLF and VIRGO data. Kiefer et al. (2018) reported on the variation of these mode parameters for the GONG instruments over two solar cycles. The increase in mode linewidth is related to the decreasing size of granulation that drives the excitation mechanism of the modes (Kiefer et al. 2018). Such variations in granular size with solar activity were indeed measured by Ballot et al. (2021) but with a one-year delay. Changes in linewidths using VIRGO/SPM data were also reported by Toutain & Kosovichev (2005) during half a solar cycle. Hereafter, I report on variations over two solar cycles taking into account the varying duty cycle in the data.

6.2.1. Impact of gaps

When measuring linewidths and mode heights, one has to take care about how the power is redistributed in the power spectrum. When there are gaps in the data, the frequency bins become correlated (Gabriel 1994). The influence of such gaps in the power spectrum can be corrected by properly taking account the statistics as shown by Stahn & Gizon (2008). In practice, the power spectrum fitting is done assuming that the frequency bins are not correlated resulting in biasing the mode linewidth as shown by Komm et al. (2000a) for the GONG data, or by Chaplin et al. (2000) for the BiSON data. For studying the impact of gaps on the mode linewidth and mode height, I created 29 times series using the first year as a reference, then applied the data gap structure of each time series to the reference time series, thereby creating 28 new time series. I averaged the mode linewidth and mode height over the frequency range from 2400 μHz to 3500 μHz (as for frequency), and over the degrees. I did a straight average between over the frequency range, not using the weighting scheme of Chaplin et al. (2004). Figure 13 provides the variation of the mean mode linewidth and mean mode height as a function of the gap fraction, together with a linear fit

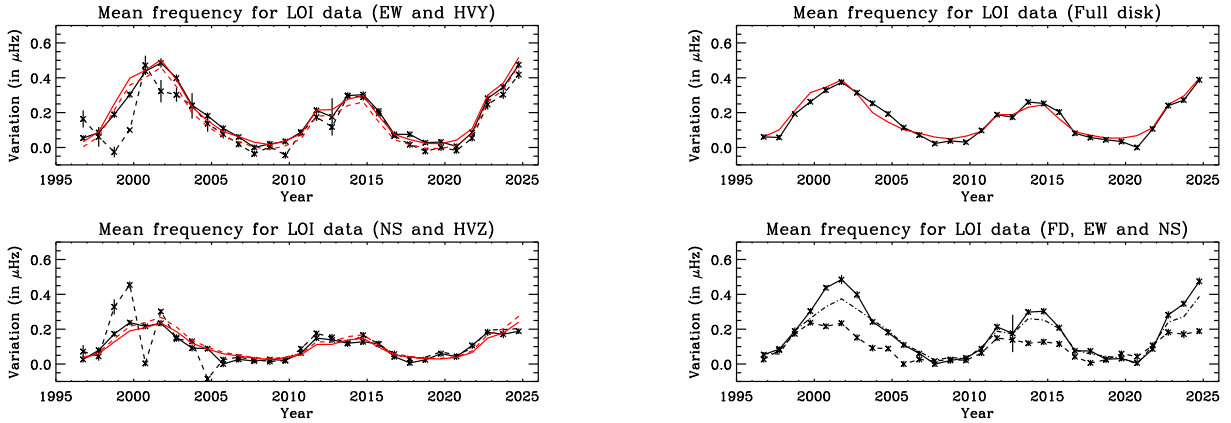


Fig. 9. Mean mode frequency variation as a function of time. (Top, left) averaged over the $l = 1$ and 2 modes for the EW difference (continuous line), for the EW HV (dashed line), and the respective fits of the variations to the F10.7 cm flux (in red). (Top, right) averaged over the $l = 0, 1$ and 2 modes for the global fit of the FD data (continuous line) and the fit of the variations to the F10.7 cm flux (red line). (Bottom, left) averaged over the $l = 1$ and 2 modes for the NS difference (continuous line), for the NS HV (dashed line), and the respective fits of the variations to the F10.7 cm flux (in red) (bottom, right) for comparison: the averaged EW difference signal (continuous line), the averaged NS difference signal (dashed line) and the averaged FD signal (dash-dotted line).

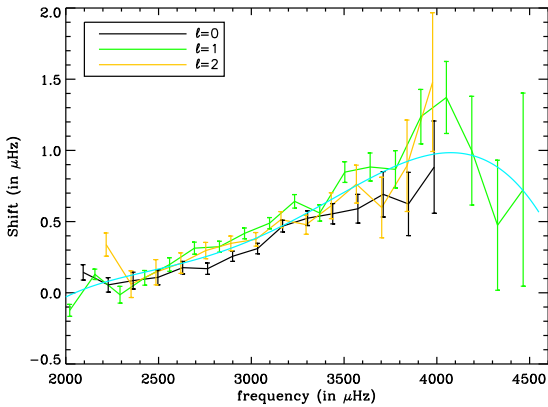


Fig. 10. Frequency shifts as a function of frequency between maximum and minimum activity for various degree. The cyan line is a fourth-order polynomial fit of the three shifts.

of the dependence. On average for any 1% additional gap, the mode linewidth is increased by 0.85%, while the mode height is reduced by 2.1%. Values of the same order of magnitude were found by [Keith-Hardy et al. \(2019\)](#) for the GONG data. The impact of gap on linewidth and height is the direct result of the dilution of power due the widening of the window function ([Gabriel 1994](#)). The dependence was used for compensating the effect of gaps on the mean mode linewidth and height (see Section 6.2.3).

6.2.2. Linewidth dependence on the degree and frequency

Using the resolved data, I inferred the dependence of the mode linewidth on the 10.7 cm flux as a function of frequency. Then I computed a linear fit of the mode linewidth variation to the 10.7 cm flux. Figure 14 shows the slope as a function of frequency for $l = 1-3$. It confirms that the mode linewidth depen-

dence to activity is different from that of the frequency dependence (see Fig. 10), confirming what [Kiefer et al. \(2018\)](#) found with the GONG data.

6.2.3. Degree and frequency averaging

I averaged the mode linewidth and mode height over the frequency range [2400, 3500] μHz , and over the degrees. I did a straight average between over the frequency range, not using the frequency weighting scheme of [Chaplin et al. \(2004\)](#). Figure 15 shows the variation obtained over the solar cycle for mode linewidth, height, power and energy rate. In Figure 15, I also show the variations of the linewidth measured with a fixed background but corrected for the effect of biases due to the different background and splitting; the procedure is the same as followed by [Appourchaux et al. \(2014\)](#). One can see that the biases are indeed corrected by the procedure and that the variations follow the same trend with solar activity. The linewidth variations are correlated with the activity while the mode height and power are anti-correlated. The energy rate is independent of solar activity. The same results were observed by [Broomhall et al. \(2015\)](#) and [Kiefer et al. \(2018\)](#) with the BiSON and GONG data, respectively.

7. Results for the 29-year time series

I used the single time series of 29 years of the FD data for getting robust estimate of mode frequencies, linewidths and heights. Figure 16 shows the power spectrum obtained with the 29 years of FD data together with the ratio of the power spectrum to the fitted model. The regular repetition of the modes can be used to derive an échelle diagram ([Grec 1981](#)). Figure 17 shows the échelle diagram of power spectrum obtained with the 29 years of FD data together with the échelle diagram of the ratio of the power spectrum to the fitted model. The fitted model was obtained with the progFIT software. Although that software is efficient at recovering nearly all the modes, modes with low signal-to-noise ratio and narrow linewidths are not fully recovered. A Bayesian approach with the known location of these

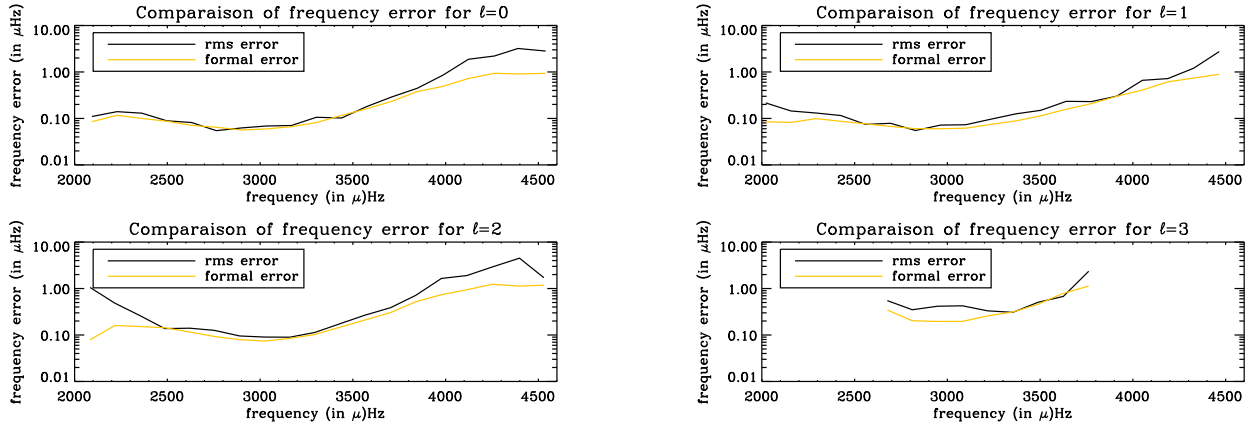


Fig. 11. Frequency error as a function of frequency: rms errors (black line), formal errors (orange line) for $l = 0$ (top, left), $l = 1$ (top, right), $l = 2$ (bottom, left) and $l = 3$ (bottom, right).

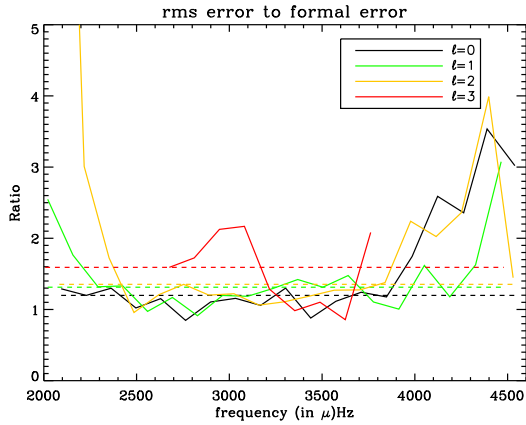


Fig. 12. Ratio of rms error to the median formal error as a function of frequency for the $l = 0, 1, 2$ and 3 modes observed in FD.

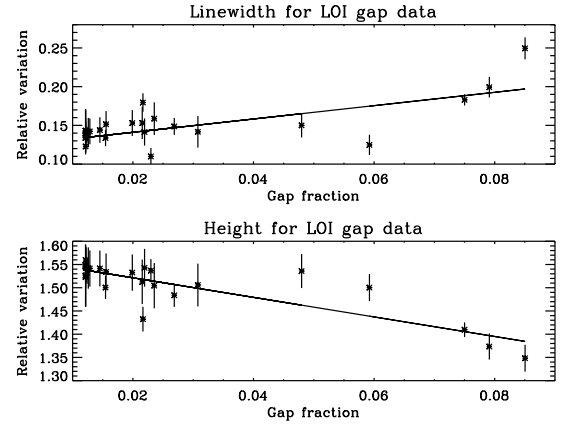


Fig. 13. Log of mean mode linewidth (top) and mean mode height (bottom) as a function of gap fraction (crosses). Linear fits are also shown (black line).

low-frequency modes (derived from velocity instrument such as GOLF) is more efficient. In addition, it has been demonstrated that there is an optimal way to smooth the power spectrum for increasing the detectability of low-frequency modes (Appourchaux 2004).

Combining the collapsogram technique (Appourchaux 2024; Salabert et al. 2009) and the smoothing of the power spectrum, I could detect modes below $1800 \mu\text{Hz}$ (see Figure 18). I used the collapsogram technique together with an optimization of the a_1 -, a_3 - and a_5 -splitting coefficients. The optimization was performed with a genetic algorithm already used by Appourchaux (2020) taking into account the statistics of the maximum (See Appourchaux 2024). After the optimization, the resulting collapsed power spectrum was fitted using MLE. As shown by Appourchaux (2003), the fitting of averaged power spectrum can be performed using the MLE technique for two degrees of freedom (d.o.f), but scaling of the error bars is required to take into account the number of d.o.f. Table E.1 gives the frequencies obtained by globally fitting the power spectrum of the 29-year time series, while Table E.2 provides the frequencies obtained at low frequency using the collapsogram.

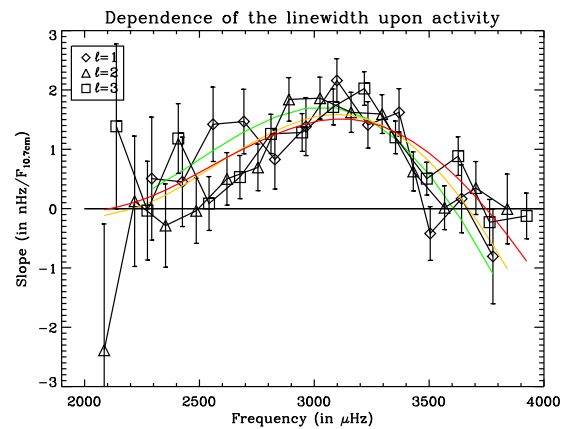


Fig. 14. Slope of the dependence of the linewidth to the 10.7 cm flux as a function of frequency for degrees $l = 1, 2$ and 3 . A second-order polynomial fit is shown for each degree: $l = 1$ (green line), $l = 2$ (orange line), and $l = 3$ (red line). The data used were the resolved data locally fitted.

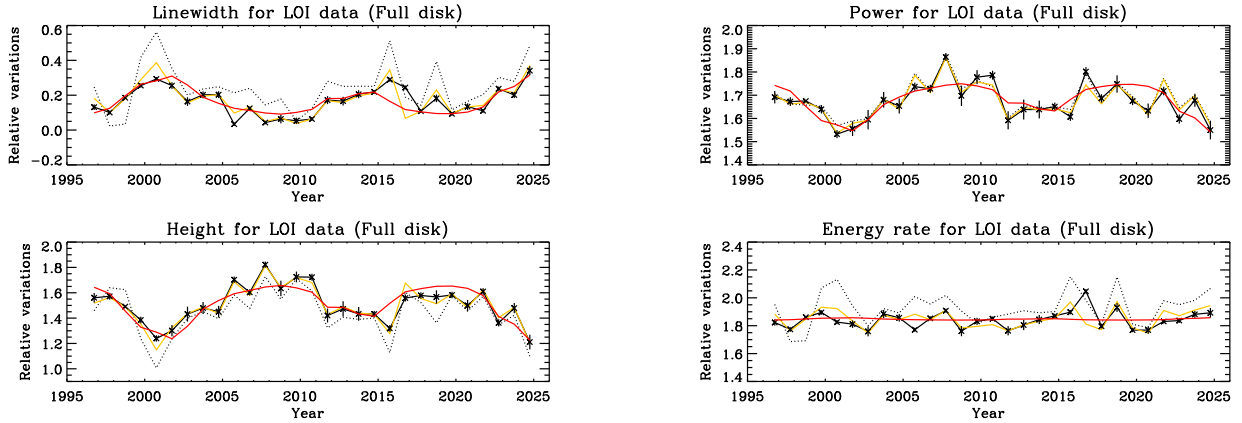


Fig. 15. Mode parameter variation as a function of time for linewidth. (Top, left), power (top, right), height (bottom, left) and energy rate (bottom, right). The continuous black line is for the globally fitted data with a free background, while the dotted line is for a fixed background. The correction of the parameters obtained for a fixed background is shown as an orange line; the correction is performed like in Appourchaux et al. (2014). The red lines shows the linear fit of each parameter to the 10.7 cm flux.

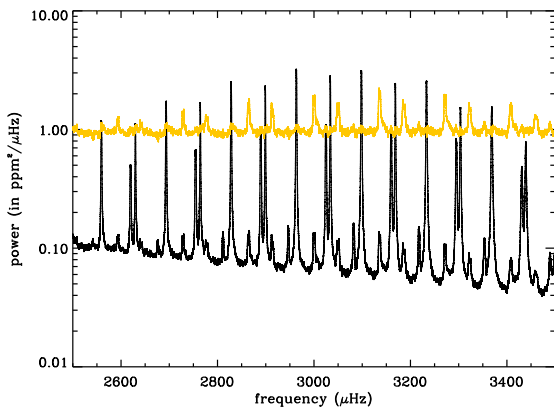


Fig. 16. Power spectrum as a function of frequency for 29 years (black line); ratio of the power spectrum to that of the fitted mode as a function of frequency (orange line) showing the remaining modes not included in the model. The remaining $l = 4$ modes are located on the left side of the $l = 0-2$ pair, while the remaining $l = 5$ modes with a lower amplitude are located on the right side of the $l = 0-2$ pair. (see also Fig. 17).

Figure 19 gives the mode linewidth and mode height obtained using the global fit and the collapsogram (see Tables F.1 and F.2). Since the averaging is performed over nearly 2 solar cycles with varying linewidths and frequency shifting, the mode linewidths are slightly higher than at low activity. The impact of the frequency shift upon the linewidth was studied by Chaplin et al. (2008) but not taking into account the variation of the linewidth; the typical overestimation they obtained over a solar cycle for the linewidth were less than 3%. For taking into account the change of all parameters over the solar cycle, I simulated the impact of the variations using the measured mode frequency, linewidth and height variations. I created 29 yearly time series for a single p mode to obtain a time series spanning the two solar cycles. Each time series has an injected frequency shift according to Fig. 10 and a linewidth and height changes according to Fig. 14, all scaled to the 10.7 cm flux. I fitted the resulting power spectrum for four typical fre-

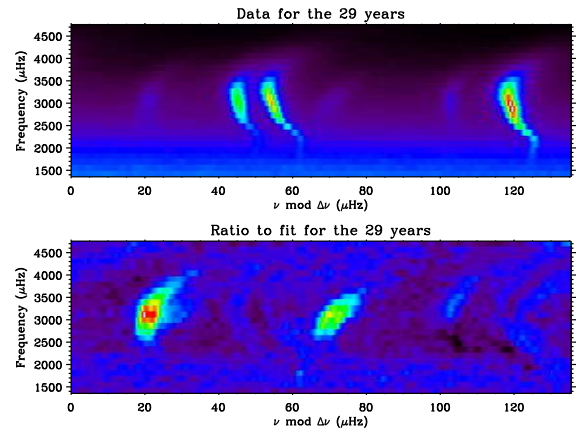


Fig. 17. (Top) Echelle diagram of the power spectrum for 29 years of LOI FD data. The double ridges close to the centre are the $l = 0-2$ modes, while the ridge on the right side are the $l = 1$ modes, sided by the faint ridge of the $l = 3$ modes. (bottom) Echelle diagram of the ratio of the power spectrum to that of the fitted model for 29 years. The remaining ridge on the left side are the $l = 4$ modes, with a faint ridge of the $l = 7$ modes going through. The remaining ridge at the center are the $l = 5$ modes.

quencies: 2500 μHz , 3000 μHz , 3500 μHz , 4000 μHz . While the resulting fitted frequency shift is the same as the mean injected frequency shifts (averaged over the 29 time series), the mode linewidth variations are about 30% larger, i.e. the linewidth are 5% and 10% larger, at 2500/3500 μHz and 3000 μHz ; there is no impact at 4000 μHz as there is no resulting mode linewidth variation (see Figure 14). Therefore, the resulting simulated bias on linewidth is only related to the linewidth variation with a typical frequency dependence similar to that of Figure 14. Despite this bias, the mode linewidths are in good agreement with measurements obtained by BiSON (Chaplin et al. 1997; Davies et al. 2014), GOLF (Gelly et al. 2002), GONG (Komm et al. 2000b; Korzennik 2023), HMI (Korzennik 2023) and VIRGO/SPM (García et al. 2011). I note that the linewidths measured by

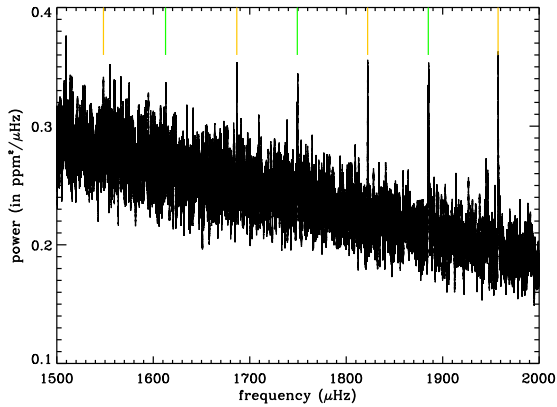


Fig. 18. power spectrum as a function of frequency for 29 years at low frequency smoothed over $0.25 \mu\text{Hz}$ (black line); the $l = 0$ and $l = 1$ mode frequencies are indicated as vertical orange and green lines, respectively. The $l = 2$ and $l = 3$ modes are fainter and not visible at low frequency.

Komm et al. (2000b) with GONG are smaller than the other measurements above $3700 \mu\text{Hz}$.

8. Results for the guiding signals

Figure 20 shows the mode heights for $l = 1$ and $l = 2$ for the various guiding signals. It is obvious that the mode heights for the HV signals are about 5–10 times larger than those of the FD and resolved signals. On the other hand, the associated linewidths as shown in Figure 21 are very similar, showing that the larger mode heights measured are not a result of a potential bias in the measured linewidths. It was already obvious when comparing Figure 6 with respect to Figure 4 that the mode height in the guiding signals was much than in the FD signals. The higher mode heights shown on Figure 20 were also observed in the MDI instrument by Toner et al. (1999), the HMI instrument and the PICARD mission by Corbard et al. (2013). They all showed that the p -mode power increases towards the limb having power larger by a factor of five, for integration over an annulus with a width of $0.5\% R_{\odot}$. Their results agree with the ratio of mode heights reported here.

9. Visibilities and visibility ratios

9.1. Limb darkening and solar radius calibration

The computation of the mode visibilities requires calibrating the limb darkening and the effective size of the solar radius on the LOI detector (see Appendix B). The calibration was done by computing the ratio of the mean of the NS pixels (1, 2, 3, 4) to the Central pixels (9, 10, 11, 12), the ratio of the mean of the EW pixels (5, 6, 7, 8) to the Central pixels, and the ratio of the mean of the guiding pixels (12, 13, 14, 15) as a function of the SoHO-Sun distance in AU. The computation of the relative fluxes was performed using the shape of the pixels and the presence of the tracks as provided by the manufacturer⁵. The tracks are the non-sensitive part of the detector required for getting the current resulting from the photoelectric effect. The limb darkening

is assumed to be expressed as

$$I(\mu) = (1 - u_2 - v_2) + u_2\mu + v_2\mu^2 \quad (3)$$

where $\mu = \sqrt{1 - r^2}$, and r is the distance from the Sun disk centre expressed in solar radius.

Figure D.1 shows the ratios measured during the 29 years by plotting one point per month as a function of the Sun-SoHO distance, together with the fit of these ratios. Unfortunately, this process does not allow to calibrate the limb darkening since there is a 100% correlation between the apparent solar radius and the linear (u_2) and quadratic (v_2) terms of the limb darkening. Instead, I used two sources for the limb darkening: Allen (1975) and Neckel & Labs (1994). For simplification, the limb darkening of Neckel & Labs (1994) was reduced to that of the two terms above and interpolated at 500 nm. Table 2 gives the radius of the outer dimension of the scientific pixels with respect to that of the Sun observed at 1 AU derived from the fit shown on Figure D.1. This calibration was used for deriving the visibilities for the solar p modes observed either with the scientific pixels or with the guiding pixels. I used the guiding pixel value of 0.937 ± 0.006 (Allen limb darkening).

9.2. Visibilities for the different signals

The theoretical visibilities of the p modes are directly related to the intensity perturbations which are related to the spherical harmonics and the limb darkening (See Appourchaux et al. 1998a, and Appendix B). This is correct to a first approximation but Toutain et al. (1999) showed that this approximation fails at the limb of the Sun because there the photons come from different heights in the solar atmosphere, thereby explaining the enhanced mode heights in the guiding pixels. Further developments were carried by Kostogryz et al. (2021) that included other opacity contributions in addition to that of H^- . Developments that are used for understanding the difference between intensity and velocity measurements in HMI (Fournier et al. 2025).

Using the calibrated size of the guiding pixels with respect to the Sun radius at 1 AU, I derived the theoretical visibilities for the FD, the resolved, the EW and NS difference signals, the EW and NS HV signals and the EW and NS guiding pixels. Then the theoretical ratios of visibilities were computed.

From the observations, I computed the average mode height for a given frequency over the 29 time series for all signals, as shown in Figure 20. The ratio was then computed only for the modes spanning the frequency range $[2500 \mu\text{Hz}, 3500 \mu\text{Hz}]$. The ratios were then averaged over the modes for getting the mean ratio; the error bars were deduced from the rms value divided by the square root of the number of frequencies. Tables D.1, D.2, D.3, D.4 and D.5 give the comparison between the ratio averaged over the 29 time series and the theoretical ratio at the mean SoHO-Sun distance of 0.9906 AU.

The radius of the outer boundary of the scientific pixels was also fitted in order to minimize the difference between the theoretical and observed FD ratios. The adjusted value of 0.941 ± 0.08 is very close to the value given in the previous section. This coherence gives confidence in the value of the size and shape of the pixels, and in the understanding of the impact of the SoHO-Sun distance in the mode visibilities.

The FD visibility ratios shown in Table D.1 are in good agreement for all degrees but $l = 3$. The observed visibility ratio for $l = 3$ is 3.7% of the $l = 1$ compared to a theoretical value of 2%. This is a large discrepancy that I do not study in detail but could be related to non-linearities due to the varying B angle (the

⁵ Advanced Micro Electronics, Horten, Norway.

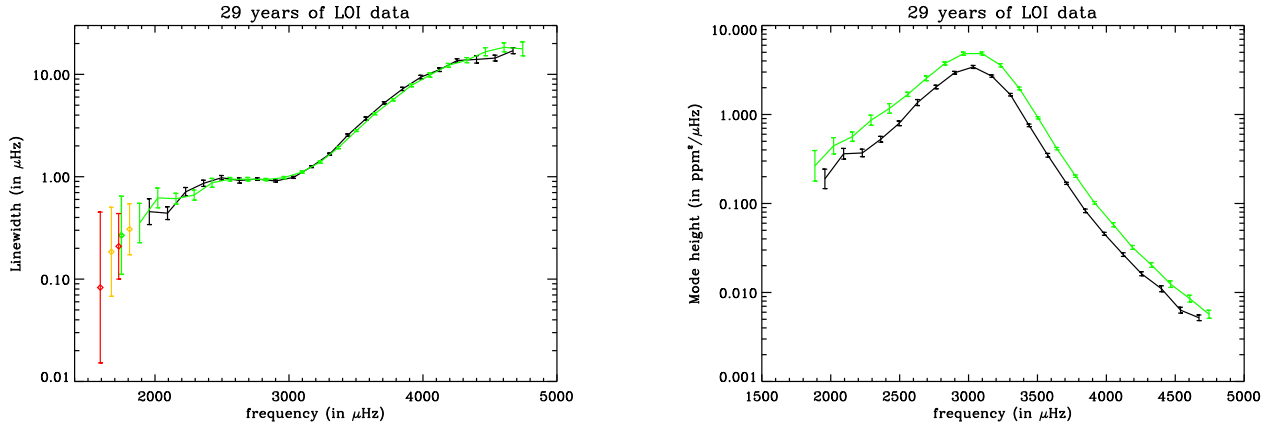


Fig. 19. (left) Mode linewidth as a function of frequency for the $l = 0-2$ doublets (black line) and for the $l = 1$ modes (green line) obtained with the global fit of the power spectrum. The linewidths at low frequencies for $l = 2$ (orange diamond) and for $l = 1$ (red diamond) were obtained using the collapsogram technique. (right) Mode height as a function of frequency for the $l = 0-2$ doublets (black line) and for the $l = 1$ modes (green line).

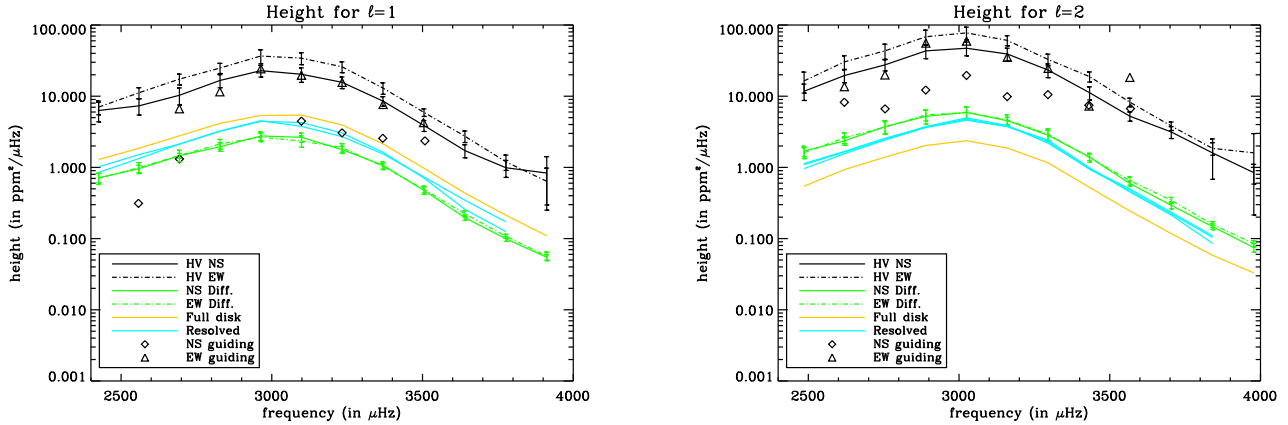


Fig. 20. Mode height as a function of frequency for the $l = 1$ modes (left) and for the $l = 2$ modes (right) for different signals: north-south high-voltage (continuous line), east-west high-voltage (Dash-dotted line), north-south scientific pixels difference (green continuous line), east-west scientific pixels difference (green dash-dot line), FD (orange line), resolved (cyan line), north-south guiding pixels (diamond), east-west guiding pixels (triangle). For the $l = 1$ resolved data, the mode heights for $m = 0$ are superimposed on those of the $m = \pm 1$ after correction of the visibilities. For the $l = 2$ resolved data, the mode heights for $m = 0, \pm 1$ are superimposed on those of the $m = \pm 2$ after correction of the visibilities.

inclination of the solar axis towards the observer). The visibility ratios of Table D.1 are different from those of Ballot et al. (2011) mainly because of the presence of tracks in the FD signal of the LOI, not present in true Sun-as-a-star signals (the track size is about 1.6% of the radius of the solar image).

The resolved visibility ratios shown in Table D.2 are also in good agreement within a multiplet, while there is a systematic bias of about 19% with respect to the FD visibilities. The EW and NS difference signal visibility ratios shown in Table D.3 are in very good agreement showing no discrepancy.

Finally, the visibility ratios for the EW and NS signals (guiding pixels and HV) are given in Table D.4 showing very large discrepancies that are also clear in Figure 20. The same discrepancy appears for the visibility ratios between the HV signals and the guiding pixels in Table D.5. One can see that the theoretical visibilities for the EW and NS signals (guiding pixels and HV) for a given degree are identical, as demonstrated in Appendix C, then so are the ratios of visibilities. I

discuss the implication of these observed visibilities in the last section.

10. Discussion and conclusion

For this article, I studied 29 years of observations of the LOI instrument on board SoHO. I corrected the impact of the so-called attractors that would lock the measured intensity flux to several digital values. The flux intensities were also corrected to take into account the roll of SoHO due to the failed mechanism of the HGA. Although the fluxes dropped by a factor of 16, the power spectrum of the Sun-as-a-star time series did not drastically change between 1996 and 2004. On the other hand, the power spectrum of the guiding pixels shows the solar p modes only in the 1996 time series. After 1997, the noise is so high that the modes cannot be detected in the guiding pixels anymore. Surprisingly, the HV signals for the EW and NS directions are

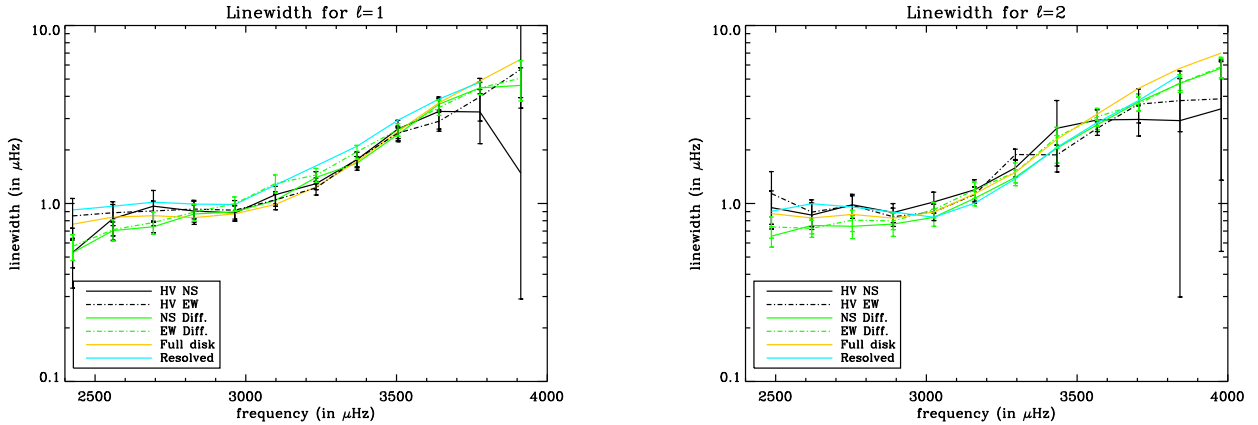


Fig. 21. Mode linewidth as a function of frequency for the $l = 1$ modes (left) and for the $l = 2$ modes (right) for different signals: north-south high-voltage (continuous line), east-west high-voltage (Dash-dotted line), north-south scientific pixels difference (green continuous line), east-west scientific pixels difference (green dash-dotted line), FD (orange line), resolved (cyan line).

Table 2. Apparent radius of the outer dimension of the scientific pixels relative to the solar radius at 1 AU for two different limb darkenings derived from the fit of the ratio of pixel flux.

Source	u_2	v_2	radius (NS)	radius (EW)	radius (guiding)
Allen (1975)	0.9700	-0.2200	0.941 ± 0.014	0.945 ± 0.014	0.937 ± 0.006
Neckel & Labs (1994)	0.9494	-0.2080	0.943 ± 0.014	0.947 ± 0.014	0.938 ± 0.006

much less noisy between 1996 and 2024; typically the noise signals became about four times lower making the detection of p modes much easier. Using C++ codes developed for the PLATO mission, I globally fitted the power spectra of the various signals.

I studied the effect of solar activity upon mode frequency, mode linewidths and mode heights for various signals. I confirm the previous finding on the dependence of frequency with solar activity which is similar to the surface frequency effect. These results are new; this is the first time that they have been published for intensity measurements. The impact of the a_2 -coefficients upon the frequency shift of the different signals have an implication for the measurement of the frequency shift in other stars (Also studied by Benomar et al. 2023). The NS difference or NS HV mimics the observations of star having a rotation axis inclined pole-on (inclination angle of 0), while the EW difference or EW HV mimics that of a star observed with the rotation axis in the plane of the sky. The difference between the frequency shift is larger for the EW signals than for the NS signals. For any other inclination angle the frequency shift will vary between these two extremes. In other words, the level of activity as measured with the frequency shift depends upon the inclination angle. Extreme care must be taken when drawing conclusions on stellar activity with stars of similar age, radius, and mass. This may affect stellar activity studies performed with PLATO (Rauer et al. 2025).

I also studied the heights of the modes detected in the guiding pixels and HV signals. The mode heights in the HV guiding signals are about 5–10 times larger than the modes observed in FD for $l = 1$, while it is about ten to twenty times larger for $l = 2$ (after correction of the $l = 2$ FD visibility). These higher mode heights are in agreement with other observations performed by Toner et al. (1999) and Corbard et al. (2013) with MDI, HMI and the PICARD mission. On the other hand, the

visibility ratios for the EW and NS signals (guiding pixels and HV) reported in this article are clearly not in agreement with the expectation of the simple theory provided in Appendix C. There are several discrepancies with theory to be noted (see Tables D.4 and D.5): 1) the mode visibilities of the EW signals are systematically higher than those of the NS signals; 2) the mode visibilities of the $l = 2$ modes are significantly higher than those of the $l = 1$ modes for the guiding pixels and the HV signals. If one compares the results of the HV signals with the EW and NS difference (see Table D.3), it is clear that for these latter signals that the mode visibilities in EW and NS are identical for $l = 1$ and $l = 2$ and that the ratio of mode visibilities of the $l = 2$ to the $l = 1$ modes are in agreement with theory. It means that the intensity perturbation at the centre of the disk ($\mu = 1$) down to $\mu = \sqrt{1 - 0.941^2} = 0.338$ follows a product of the limb darkening with a spherical harmonic (Eq. (C.1)).

When this is not the case, one can use the formalism given by Toutain et al. (1999) for deriving the visibility ratio of $l = 2$ with respect to $l = 1$. I show in Appendix C that the ratio of these visibilities for either the EW or NS signals is $(\Delta^{21}/\Delta^{11})^2$. For spherical harmonics perturbations, this ratio is about 0.2 (see Table D.4). Using the relative intensity perturbation provided by Toutain et al. (1999) in their Figures 5 and 6 for $l = 2, m = 1$ (used for Δ^{21}) and for $l = 1, m = 1$ (used for Δ^{11}), one can deduce that the ratio $(\Delta^{21}/\Delta^{11})^2$ should be much less than 1 as well. The intensity perturbations provided by Toutain et al. (1999) do not contradict the simple theory provided by Table D.4. The theory of Toutain et al. (1999) was revised by Prokhorov et al. (2014) and Kostogryz et al. (2021). The latter used additional opacity in addition to the sole contribution of bound-free transitions of H^- included in the model of Toutain et al. (1999). Unfortunately, Kostogryz et al. (2021) did not provide the intensity perturbations for $l = 1$ and $l = 2$. The computation of such perturbation

using the methodology of Kostogryz et al. (2021) is beyond the scope of the current article.

This work may also serve future purposes for showing what can be achieved with a low-resolution instrument detecting p modes in other stars. To date, the observations of stellar p modes by CoRoT (Baglin 2006), Kepler (Gilliland et al. 2010), TESS (Ricker et al. 2014) and the future PLATO (Rauer et al. 2025) missions only allow the detection of low degree modes below $l = 3$. In the future, we hope to have large interferometers in space such as the concept of the Stellar Imager proposed by Carpenter et al. (2010), which was aimed at providing about 30 resolution elements across a star ($l < 10$). It would require the formation flying of 30 telescopes of 2 m in diameter on a kilometre baseline. Such challenging developments are not impossible as a realistic road map for formation flying for space-based interferometry has been devised (Monnier et al. 2019).

Finally, this work will be used as the reference for the data reduction of the LOI instrument for which data will be archived at the European Space Astronomy Centre (ESAC) in Villafranca, Spain in the SOHO data archive. At the time of writing, the end of the SoHO mission is planned for September 2026 (D. Müller, private communication).

Acknowledgements. This article benefited from fruitful discussions I had with Bo Andersen, Antonio Jiménez and Torben Leifsen held during a memorable meeting in Svalbard. This article represents the work performed during 3/4 of my career during which I owe a lot to several of my forefathers: Jacques-Emile Blamont who introduced to the world of helioseismology and political maneuvering; Pierre Connes who introduced to the world of well-thought instrumentation, of spectroscopy and exoplanet search; David M. Rust who had more faith and confidence in me that I will ever have which enabled me to be more aware of what I could do; Claus Fröhlich who permitted me to be in charge and to develop the LOI instrument. I owe a lot also to my career-long colleagues: Bo N. Andersen who was at the start of the LOI concept, long standing friend whatever the circumstances; Antonio Jiménez still kicking the VIRGO Data Centre and provider of the Level 0 data. I owe also to the many ESTEC engineers that allowed me to design, to develop, to test the LOI especially Udo Telljohann. Last but not least, I could not have done this career without the long time support of my wife, Maryse, there since the university years; my two sons, Kévin and Thibault, and our many gone or still-living cats. A special mention to Roger-Maurice Bonnet, Alan Gabriel and Jean-Claude Vial for permitting me to go back to instrumentation development in France. SoHO is a mission of international collaboration between ESA and NASA. The development of the progFIT code was initiated by Bernard Leroy and Coralie Neiner at my prodding, code which was transformed into a regularly usable code with the major contribution of Claude Mercier, and the timely contribution of Vincent Buttice.

References

- Allen, C. W. 1975, *Astrophysical Quantities* (The Athlone Press)
- Andersen, B. N., Domingo, V., Jones, A., et al. 1988, in *Seismology of the Sun and Sun-like Stars*, eds. V. Domingo, & E. Rolfe, (Noordwijk, The Netherlands: ESA SP-286, ESA Publications Division), 385
- Antia, H. M., Basu, S., Hill, F., et al. 2001, *MNRAS*, **327**, 1029
- Appourchaux, T. 2003, *A&A*, **412**, 903
- Appourchaux, T. 2004, *A&A*, **428**, 1039
- Appourchaux, T. 2020, *A&A*, **642**, A226
- Appourchaux, T. 2024, *Sol. Phys.*, **299**, 155
- Appourchaux, T., & Andersen, B. N. 1990, *Sol. Phys.*, **128**, 91
- Appourchaux, T., & Chaplin, W. J. 2007, *A&A*, **469**, 1151
- Appourchaux, T., & Toutain, T. 1998, in *Sounding Solar and Stellar Interiors*, IAU 181, *Poster volume*, eds. J. Provost, & F.-X. Schmider (Dordrecht: Kluwer Academic Publishers), 5
- Appourchaux, T., Toutain, T., Telljohann, U., et al. 1995, *A&A*, **294**, L13
- Appourchaux, T., Andersen, B. N., Fröhlich, C., et al. 1997, *Sol. Phys.*, **170**, 27
- Appourchaux, T., Gizon, L., & Rabello-Soares, M. C. 1998a, *A&AS*, **132**, 107
- Appourchaux, T., Rabello Soares, M. C., & Gizon, L. 1998b, *IAU Symp.*, **185**, 167
- Appourchaux, T., Rabello-Soares, M.-C., & Gizon, L. 1998c, *A&AS*, **132**, 121
- Appourchaux, T., Fröhlich, C., Andersen, B. N., et al. 2000, *ApJ*, **538**, 401
- Appourchaux, T., Andersen, B., & Sekii, T. 2002, *ESA SP*, **508**, 47
- Appourchaux, T., Leibacher, J., & Boumier, P. 2007, *A&A*, **463**, 1211
- Appourchaux, T., Michel, E., Auvergne, M., et al. 2008, *A&A*, **488**, 705
- Appourchaux, T., Belkacem, K., Broomhall, A.-M., et al. 2010, *A&ARv*, **18**, 197
- Appourchaux, T., Antia, H. M., Benomar, O., et al. 2014, *A&A*, **566**, A20
- Baglin, A. 2006, in *The CoRoT Mission, Pre-launch Status, Stellar Seismology and Planet Finding*, eds. M. Fridlund, A. Baglin, J. Lochard, & L. Conroy (Noordwijk, The Netherlands: ESA SP-1306, ESA Publication Division)
- Ballot, J., Barban, C., & van't Veer-Menneret, C. 2011, *A&A*, **531**, A124
- Ballot, J., Roudier, T., Malherbe, J. M., & Frank, Z. 2021, *A&A*, **652**, A103
- Benomar, O., Appourchaux, T., & Baudin, F. 2009, *A&A*, **506**, 15
- Benomar, O., Takata, M., Bazot, M., et al. 2023, *A&A*, **680**, A27
- Broomhall, A. M., Chaplin, W. J., Elsworth, Y., & Appourchaux, T. 2007, *MNRAS*, **379**, 2
- Broomhall, A. M., Pugh, C. E., & Nakariakov, V. M. 2015, *Adv. Space Res.*, **56**, 2706
- Carpenter, K. G., Schrijver, C. J., Karovska, M., et al. 2010, ArXiv e-prints [arXiv:1011.5214]
- Chaplin, W. J., Elsworth, Y., Isaak, G. R., et al. 1997, *MNRAS*, **288**, 623
- Chaplin, W. J., Elsworth, Y., Isaak, G. R., Miller, B. A., & New, R. 2000, *MNRAS*, **313**, 32
- Chaplin, W. J., Elsworth, Y., Isaak, G. R., Miller, B. A., & New, R. 2004, *MNRAS*, **352**, 1102
- Chaplin, W. J., Houdek, G., Appourchaux, T., et al. 2008, ArXiv e-prints [arXiv:0804.4371]
- Claverie, A., Isaak, G., McLeod, C., van der Raay, H., & Roca Cortés, T. 1979, *Nature*, **282**, 591
- Corbard, T., Salabert, D., Boumier, P., et al. 2013, *J. Phys. Conf. Ser.*, **440**, 012025
- Corsaro, E., & De Ridder, J. 2014, *A&A*, **571**, A71
- Davies, G. R., Broomhall, A. M., Chaplin, W. J., Elsworth, Y., & Hale, S. J. 2014, *MNRAS*, **439**, 2025
- Duvall, T. L., Jr., & Harvey, J. W. 1984, *Nature*, **310**, 19
- Duvall, T. L., Jr., Dziembowski, W. A., Goode, P. R., et al. 1984, *Nature*, **310**, 22
- Echeverria, A., Silva, J. F., Mendez, R. A., & Orchard, M. 2016, *A&A*, **594**, A111
- Elsworth, Y., Howe, R., Isaak, G. R., McLeod, C. P., & New, R. 1991, *MNRAS*, **251**, 7P
- Fossat, E. 1991, *Sol. Phys.*, **133**, 1
- Fournier, D., Kostogryz, N., Gizon, L., et al. 2025, *A&A*, **702**, A253
- Fröhlich, C., & Van der Raay, H. B. 1984, in *The Hydromagnetics of the Sun*, eds. T. D. Guyenne, & J. J. Hunt (Noordwijk, The Netherlands: ESA SP-220, ESA Publications Division), 17
- Fröhlich, C., Bonnet, R. M., Bruns, A. V., et al. 1988, in *Seismology of the Sun and Sun-Like Stars*, eds. V. Domingo, & E. Rolfe, (Noordwijk, The Netherlands: ESA SP-286, ESA Publications Division), 359
- Fröhlich, C., Romero, J., Roth, H., et al. 1995, *Sol. Phys.*, **162**, 101
- Gabriel, M. 1994, *A&A*, **287**, 685
- Gabriel, A. H., Grec, G., Charra, J., et al. 1995, *Sol. Phys.*, **162**, 61
- García, R. A., Salabert, D., Ballot, J., et al. 2011, *J. Phys. Conf. Ser.*, **271**, 012049
- Gelly, B., Lazrek, M., Grec, G., et al. 2002, *A&A*, **394**, 285
- Gilliland, R. L., Brown, T. M., Christensen-Dalsgaard, J., et al. 2010, *PASP*, **122**, 131
- Gizon, L., Appourchaux, T., & Gough, D. O. 1998, in *New eyes to see inside the sun and the stars*, IAU 185, eds. F.-L. Deubner, J. Christensen-Dalsgaard, & D. Kurtz (Dordrecht, The Netherlands: Kluwer Academic Publishers), 185, 37
- Gough, D. O. 1984, *Roy. Soc. Lond. Philos. Trans. Ser.*, **313**, 27
- Gould, B. A. 1855, *AJ*, **4**, 81
- Grec, G. 1981, Ph.D. Thesis, Université de Nice
- Grec, G., Fossat, E., & Pomerantz, M. 1980, *Nature*, **288**, 541
- Handberg, R., & Campante, T. L. 2011, *A&A*, **527**, A56
- Howe, R., Chaplin, W. J., Elsworth, Y. P., Hale, S. J., & Nielsen, M. B. 2023, *MNRAS*, **526**, 1447
- Jiménez-Reyes, S. J., García, R. A., Jiménez, A., & Chaplin, W. J. 2003, *ApJ*, **595**, 446
- Keith-Hardy, J. Z., Tripathy, S. C., & Jain, K. 2019, *ApJ*, **877**, 148
- Kiefer, R., Komm, R., Hill, F., Broomhall, A.-M., & Roth, M. 2018, *Sol. Phys.*, **293**, 151
- Komm, R. W., Howe, R., & Hill, F. 2000a, *ApJ*, **531**, 1094
- Komm, R. W., Howe, R., & Hill, F. 2000b, *ApJ*, **543**, 472
- Korzennik, S. G. 2023, *Front. Astron. Space Sci.*, **9**, 1031313
- Kosovichev, A. G., Christensen-Dalsgaard, J., Daepfen, W., et al. 1992, *MNRAS*, **259**, 536
- Kostogryz, N. M., Fournier, D., & Gizon, L. 2021, *A&A*, **654**, A1
- Libbrecht, K. G., & Woodard, M. F. 1990, *Nature*, **345**, 779
- Lund, M. N., Silva Aguirre, V., Davies, G. R., et al. 2017, *ApJ*, **835**, 172
- Monnier, J. D., Aarnio, A., Absil, O., et al. 2019, ArXiv e-prints [arXiv:1907.09583]

- Neckel, H., & Labs, D. 1994, [Sol. Phys.](#), **153**, 91
- Neiner, C., & Appourchaux, T. 2004, [ESA SP](#), **538**, 373
- Peirce, B. 1852, [AJ](#), **2**, 161
- Prokhorov, A., Zhugzhda, Y. D., & Berdyugina, S. 2014, [Astron. Nachr.](#), **335**, 150
- Rauer, H., Aerts, C., Cabrera, J., et al. 2025, [Exp. Astron.](#), **59**, 26
- Ricker, G. R., Winn, J. N., Vanderspek, R., et al. 2014, [J. Astron. Telesc. Instrum. Syst.](#), **1**, 014003
- Ritzwoller, M. H., & Lavelly, E. M. 1991, [ApJ](#), **369**, 557
- Salabert, D., Leibacher, J., Appourchaux, T., & Hill, F. 2009, [ApJ](#), **696**, 653
- Scherrer, P. H., Bogart, R. S., Bush, R. I., et al. 1995, [Sol. Phys.](#), **162**, 129
- Scherrer, P. H., Schou, J., Bush, R. I., et al. 2012, [Sol. Phys.](#), **275**, 207
- Schou, J. 1992, Ph.D. Thesis, Århus Universitet, Denmark
- Schou, J., Howe, R., Basu, S., et al. 2002, [ApJ](#), **567**, 1234
- Siddiqi, A. 2016, Beyond Earth – A Chronicle of deep space exploration, 1958–2016, NASA SP-2018-4041, Tech. rep., National Aeronautics and Space Administration
- Stahn, T., & Gizon, L. 2008, [Sol. Phys.](#), **251**, 31
- Toner, C. G., Jefferies, S. M., & Toutain, T. 1999, [ApJ](#), **518**, L127
- Toutain, T., & Fröhlich, C. 1992, [A&A](#), **257**, 287
- Toutain, T., & Gouttebroze, P. 1993, [A&A](#), **268**, 309
- Toutain, T., & Kosovichev, A. G. 2005, [ApJ](#), **622**, 1314
- Toutain, T., Appourchaux, T., Baudin, F., et al. 1997, [Sol. Phys.](#), **175**, 311
- Toutain, T., Appourchaux, T., Fröhlich, C., et al. 1998, [ApJ](#), **506**, L147
- Toutain, T., Berthomieu, G., & Provost, J. 1999, [A&A](#), **344**, 188
- Van Trees, H. L. 1968, Inc., New York
- Vasilyev, V., & Gizon, L. 2024, [A&A](#), **682**, A142
- Willson, R. C. 1979, [Appl. Opt.](#), **18**, 179
- Woodard, M., & Hudson, H. 1983, [Sol. Phys.](#), **82**, 67

Appendix A: Clebsh-Gordan expansion of the mode splitting

In the early days of helioseismology (before the 1990s), mode splittings were usually expressed in term of Legendre polynomials. Unfortunately, these polynomials are orthogonal only on a continuous space (between $[-1,1]$) not on a discrete set such as $(-1, 0, +1)$ for $l=1$, for example. Therefore, other expansion are required that can either be computed by hand or derived from quantum mechanics. Ritzwoller & Lavelly (1991) derived these polynomials from quantum mechanics and used a normalization such that even for high degree modes their a_1 are asymptotically equal to the usual Legendre polynomials. It is now common practice to have a normalization such that this is the case. The splittings are expressed as

$$\nu_{(l,m)} - \nu_{(l,0)} = \sum_{i=1}^{i=n} a_i l \mathcal{P}_l^i(m) \quad (\text{A.1})$$

where l is the degree, m the order, and selected $\mathcal{P}_l^i(m)$ are given as

$$\mathcal{P}_l^1(m) = \frac{m}{l} \quad (\text{A.2})$$

$$\mathcal{P}_l^2(m) = \frac{6m^2 - 2L^2}{6l^2 - 2L^2} \quad (\text{A.3})$$

$$\mathcal{P}_l^3(m) = \frac{20m^3 - 4m(3L^2 - 1)}{20l^3 - 4l(3L^2 - 1)} \quad (\text{A.4})$$

$$\mathcal{P}_l^4(m) = \frac{70m^4 - 10m^2(6L^2 - 5) + 6L^2(L^2 - 2)}{70l^4 - 10l^2(6L^2 - 5) + 6L^2(L^2 - 2)} \quad (\text{A.5})$$

$$\mathcal{P}_l^5(m) = \frac{252m^5 - 140(2L^2 - 3)m^3 + (20L^2(3L^2 - 10) + 48)}{252l^5 - 140(2L^2 - 3)l^3 + (20L^2(3L^2 - 10) + 48)} \quad (\text{A.6})$$

with $L^2 = l(l + 1)$. I note that for all i we have $\mathcal{P}_l^i(l) = 1$. The polynomials are derived from Eqs (39) to (44) of Ritzwoller & Lavelly (1991).

Appendix B: LOI visibilities

The LOI visibilities are written as

$$S_{nlm} = \sqrt{\frac{1}{N} \sum_{i=1}^{i=N} \tilde{y}_i^{(l,m)*} \tilde{y}_i^{(l,m)}} \quad (\text{B.1})$$

where N is the number of pixels, and $\tilde{y}_i^{(l,m)}$ are given by

$$\tilde{y}_i^{(l,m)} = \frac{\int_{\mathcal{D}_i} \sqrt{4\pi} Y_l^m(\theta, \phi) I(\sin \theta \cos \phi) \sin^2 \theta \cos \phi d\theta d\phi}{\int_{\mathcal{D}_i} I(\sin \theta \cos \phi) \sin^2 \theta \cos \phi d\theta d\phi} \quad (\text{B.2})$$

where \mathcal{D}_i is the domain representing pixel i ; $Y_l^m(\theta, \phi)$ is the spherical harmonic with (θ, ϕ) the spherical angular coordinates of a point on the surface of the Sun and I is the limb darkening.

I note that with the definition of Eq. (B.2), $\tilde{y}_i^{l,m} = 1$, and therefore the visibility of the LOI data for $l = 0, m = 0$ is simply $\sqrt{12/12} = 1$.

Table B.1. Visibilities of the LOI instrument

l	m	S_{nlm}
0	0	1.000
1	0	0.749
1	1	1.069
2	0	0.744
2	1	0.877
2	2	1.045
3	0	0.695
3	1	0.783
3	2	0.857
3	3	0.983

Appendix C: HV guiding signals and guiding pixel visibilities

The HV guiding signals are proportional to the difference in the guiding pixel fluxes (EW or NS). Therefore, for computing the ratio of visibilities for the HV guiding signals, one has to compute the intensity perturbation obtained from the guiding pixels.

The reference axis for spherical harmonics is linked to the solar rotation axis, x being in the direction of the observer, z being the solar rotation axis and y making the (x, y, z) axis system right-handed. The corresponding spherical coordinates are (r, θ, ϕ)

Since we are trying to integrate the flux over the guiding detectors having a circular symmetry, we use the (x', y, z') system with z' pointing toward the observer. A rotation by 90 degrees transforms the system (x, y, z) to (x', y, z') . The associated spherical coordinates are then (r', θ', ϕ') . In that framework, the east and west guiding pixels are defined by $\phi' \in [-135, -45]$ and $\phi' \in [+45, +135]$, respectively; while the north and south guiding pixels are defined by $\phi' \in [-45, +45]$ and $\phi' \in [+135, +225]$.

C.1. Intensity perturbation

Assuming that the intensity perturbation is proportional to the spherical harmonics, the perturbation integrated over the guiding pixels for a given (l, m) , can be written as

$$\Delta I_l^m = \int_{\theta'} \int_{\phi'} Y_l^m(\theta, \phi) I_{LD}(\sin \theta \cos \theta) d\Sigma \quad (\text{C.1})$$

where $d\Sigma$ is the projected surface element, (θ, ϕ) are the spherical angular coordinates, and I_{LD} is the limb darkening. The spherical harmonics expressed in the (x, y, z) system can be decomposed using Edmonds rotation matrices $D^{(l)}(\mathcal{R})$ as a function of spherical harmonics expressed in the (x', y, z') system as

$$Y_l^m(\theta, \phi) = \sum_{m'=-l}^{m'=+l} D_{mm'}^{(l)}(\mathcal{R}) Y_l^{m'}(\theta', \phi') \quad (\text{C.2})$$

Since we also have the following expression :

$$Y_l^{m'}(\theta', \phi') = c_l^{m'} P_l^{m'}(\cos \theta') e^{im'\phi'} \quad (\text{C.3})$$

we can rewrite Eq. (C.2) as

$$Y_l^m(\theta, \phi) = \sum_{m'=-l}^{m'=+l} D_{mm'}^{(l)}(\mathcal{R}) c_l^{m'} P_l^{m'}(\cos \theta') e^{im'\phi'} \quad (\text{C.4})$$

Using Eq. (C.3) we can then rewrite Eq. (C.1) as

$$\Delta I_l^m = \int_{\theta'} \int_{\phi'} \left(\sum_{m'=-l}^{m'+l} D_{mm'}^{(l)}(\mathcal{R}) c_l^{m'} P_l^{m'}(\cos \theta') e^{im'\phi'} \right) I_{LD}(\mu) d\Sigma \quad (\text{C.5})$$

The surface element can be written as $d\Sigma = \mu d\mu d\phi'$, with $\mu = \cos \theta'$. Equation (C.5) can then be separated in θ' and ϕ' as

$$\Delta I_l^m = \sum_{m'=-l}^{m'+l} D_{mm'}^{(l)}(\mathcal{R}) \left(\int_{\theta'} c_l^{m'} P_l^{m'}(\mu) I_{LD}(\mu) \mu d\mu \right) \left(\int_{\phi'} e^{im'\phi'} d\phi' \right) \quad (\text{C.6})$$

We can rewrite Eq. (C.6) as

$$\Delta I_l^m = \sum_{m'=-l}^{m'+l} [D_{mm'}^{(l)}(\mathcal{R})] \Delta^{lm'} \Delta J^{m'} \quad (\text{C.7})$$

with

$$\Delta J^{m'} = \int_{\phi'} e^{im'\phi'} d\phi' \quad (\text{C.8})$$

and:

$$\Delta^{lm'} = \int_{\theta'} c_l^{m'} P_l^{m'}(\mu) I_{LD}(\mu) \mu d\mu \quad (\text{C.9})$$

Since we have $P_l^{-m'}(\mu) = (-1)^{m'} P_l^{m'}(\mu)$, we also have $\Delta^{l'-m'} = (-1)^{m'} \Delta^{l'm'}$

Here I note that the perturbation used in Eq. (C.1) is supposed to be a spherical harmonic. [Toutain et al. \(1999\)](#) demonstrated that any perturbation can be decomposed using Edmonds rotations matrices. As a result, Eq. (C.7) does not only apply to spherical harmonics but to any perturbation using spherical harmonics as a base, involving its derivatives, or any other combination.

C.2. $\Delta J^{m'}$ for the E and W guiding pixels

The guiding pixel integrals can be calculated for the E and W pixels (E: $\phi' \in [-135, -45]$ and W: $\phi' \in [+45, +135]$) as

$$\Delta J_E^{m'} = (i^{m'}) \left(\frac{2 \sin m' \pi/4}{m'} \right) \quad (\text{C.10})$$

and

$$\Delta J_W^{m'} = (-1)^{m'} (i^{m'}) \left(\frac{2 \sin m' \pi/4}{m'} \right) \quad (\text{C.11})$$

C.3. $\Delta J^{m'}$ for the N and S guiding pixel

The guiding pixel integrals can be calculated for the N and S pixels (N: $\phi' \in [-45, +45]$ and S: $\phi' \in [+135, +225]$) as

$$\Delta J_N^{m'} = \left(\frac{2 \sin m' \pi/4}{m'} \right) \quad (\text{C.12})$$

and

$$\Delta J_S^{m'} = (-1)^{m'} \left(\frac{2 \sin m' \pi/4}{m'} \right) \quad (\text{C.13})$$

C.4. Rotation matrices $D^{(l)}(\mathcal{R})$

$$D^{(1)}(\mathcal{R}) = \begin{pmatrix} 1/2 & \sqrt{2}/2 & 1/2 \\ -\sqrt{2}/2 & 0 & \sqrt{2}/2 \\ 1/2 & -\sqrt{2}/2 & 1/2 \end{pmatrix} \quad (\text{C.14})$$

$$D^{(2)}(\mathcal{R}) = \begin{pmatrix} 1/4 & 1/2 & \sqrt{3}/8 & 1/2 & 1/4 \\ -1/2 & -1/2 & 0 & 1/2 & 1/2 \\ \sqrt{3}/8 & 0 & -1/2 & 0 & \sqrt{3}/8 \\ -1/2 & 1/2 & 0 & -1/2 & 1/2 \\ 1/4 & -1/2 & \sqrt{3}/8 & -1/2 & 1/4 \end{pmatrix} \quad (\text{C.15})$$

$$D^{(3)}(\mathcal{R}) = \begin{pmatrix} \frac{1}{8} & \sqrt{\frac{3}{32}} & \frac{\sqrt{15}}{8} & \frac{\sqrt{5}}{4} & \frac{\sqrt{15}}{8} & \sqrt{\frac{3}{32}} & \frac{1}{8} \\ \sqrt{\frac{3}{32}} & \frac{1}{2} & \sqrt{\frac{5}{32}} & 0 & \sqrt{\frac{5}{32}} & \frac{1}{2} & \sqrt{\frac{3}{32}} \\ \frac{\sqrt{15}}{8} & \sqrt{\frac{5}{32}} & -\frac{1}{8} & \frac{\sqrt{3}}{4} & -\frac{1}{8} & \sqrt{\frac{5}{32}} & \frac{\sqrt{15}}{8} \\ \frac{\sqrt{5}}{4} & 0 & \frac{\sqrt{3}}{4} & 0 & \frac{\sqrt{3}}{4} & 0 & \frac{\sqrt{5}}{4} \\ \frac{\sqrt{15}}{8} & -\sqrt{\frac{5}{32}} & -\frac{1}{8} & \frac{\sqrt{3}}{4} & -\frac{1}{8} & \sqrt{\frac{5}{32}} & \frac{\sqrt{15}}{8} \\ \sqrt{\frac{3}{32}} & \frac{1}{2} & -\sqrt{\frac{5}{32}} & 0 & \sqrt{\frac{5}{32}} & -\frac{1}{2} & \sqrt{\frac{3}{32}} \\ \frac{1}{8} & -\sqrt{\frac{3}{32}} & \frac{\sqrt{15}}{8} & -\frac{\sqrt{5}}{4} & \frac{\sqrt{15}}{8} & -\sqrt{\frac{3}{32}} & \frac{1}{8} \end{pmatrix} \quad (\text{C.16})$$

C.5. ΔI_l^m for the HV voltage

The HV signals are proportional to the difference in the intensity between the E (N) and W (S) pixels. Then we can write

$$\Delta I_l^m(\text{HV}_{EW}) = \Delta I_l^m(\text{E}) - \Delta I_l^m(\text{W}) \quad (\text{C.17})$$

and

$$\Delta I_l^m(\text{HV}_{NS}) = \Delta I_l^m(\text{N}) - \Delta I_l^m(\text{S}) \quad (\text{C.18})$$

Using the rotation matrices given above, Eqs. (C.10) to (C.13) and Eq. (C.7), and Tables C.1 to C.3 provide the results for Eqs. (C.17) and (C.18). Table C.4 gives the resulting visibilities in power after summing over all components in a multiplet.

C.6. ΔI_l^m for the EW and NS guiding pixels

The EW guiding pixel signals are proportional to the mean intensity of the E (N) and W (S) pixels. Then we can write

$$\Delta I_l^m(\text{EW}) = \frac{1}{2} (\Delta I_l^m(\text{E}) + \Delta I_l^m(\text{W})) \quad (\text{C.19})$$

Table C.1. Calculated $l = 1$ ΔI_l^m response for the HV guiding voltage.

Order	EW	NS
± 1	$2\sqrt{2}i\Delta^{11}$	0
0	0	$4\Delta^{11}$

Table C.2. Calculated $l = 2$ ΔI_l^m response for the HV guiding voltage.

Order	EW	NS
± 2	$2\sqrt{2}i\Delta^{21}$	0
± 1	0	$2\sqrt{2}i\Delta^{21}$
0	0	0

Table C.3. Calculated $l = 3$ ΔI_l^m response for the HV guiding voltage.

Order	EW	NS
± 3	$-\frac{\sqrt{2}}{6}i\Delta^{33} + \frac{\sqrt{30}}{2}i\Delta^{31}$	0
± 2	0	$-\frac{\sqrt{3}}{3}\Delta^{33} - \sqrt{5}\Delta^{31}$
± 1	$-\frac{\sqrt{30}}{6}i\Delta^{33} - \frac{\sqrt{2}}{2}i\Delta^{31}$	0
0	0	$-\frac{\sqrt{10}}{3}\Delta^{33} + \sqrt{6}\Delta^{31}$

Table C.4. Calculated visibilities for the HV guiding voltage.

Degree	EW	NS
1	$16(\Delta^{11})^2$	$16(\Delta^{11})^2$
2	$16(\Delta^{21})^2$	$16(\Delta^{21})^2$
3	$16(\Delta^{31})^2 + 16(\Delta^{33})^2/9$	$16(\Delta^{31})^2 + 16(\Delta^{33})^2/9$

and

$$\Delta I_l^m(NS) = \frac{1}{2}(\Delta I_l^m(N) + \Delta I_l^m(S)) \quad (\text{C.20})$$

C.7. The multiplet

C.7.1. $l=1$ modes

In this case, the $m = \pm 1$ responses for the EW / NS pixels and the HV EW signals are different from zero, while nothing is transmitted for $m = 0$. For the NS HV signal, only $m = 0$ is transmitted.

Table C.5. Calculated $l = 1$ ΔI_l^m response for the EW and NS guiding pixels.

Order	EW	NS
± 1	$\sqrt{2}\Delta^{10}\pi/2$	$\sqrt{2}\Delta^{10}\pi/2$
0	0	0

Table C.6. Calculated $l = 2$ ΔI_l^m response for EW and NS guiding pixels.

Order	EW	NS
± 2	$-\Delta^{22}/2 + \sqrt{3}\Delta^{20}\pi/4$	$\Delta^{22}/2 + \sqrt{3}\Delta^{20}\pi/4$
± 1	0	0
0	$-\sqrt{3}\Delta^{22}/2 - \Delta^{20}\pi/4$	$\sqrt{3}\Delta^{22}/2 - \Delta^{20}\pi/4$

Table C.7. Calculated visibilities for the EW and NS guiding pixels.

Degree	EW	NS
1	$(\Delta^{10})^2(\pi)^2$	$(\Delta^{10})^2(\pi)^2$
2	$5(\Delta^{22}/2)^2 + 7(\Delta^{20})^2(\frac{\pi}{4})^2$	$5(\Delta^{22}/2)^2 + 7(\Delta^{20})^2(\frac{\pi}{4})^2$

ted. The visibilities⁶ in the power spectrum for the EW signals and for the NS signals are identical.

C.7.2. $l=2$ modes

In this case, the $m = \pm 2$ responses for the EW guiding signals are different from zero, while nothing is transmitted for other m . For the NS guiding signals, only $m = \pm 1$ are transmitted. For the EW and NS pixels, the responses are different from 0 for $m = \pm 2$ and $m = 0$. The visibilities in the power spectrum for the EW signals and for the NS signals are identical.

C.7.3. $l=3$ modes

In this case, the $m = \pm 1, \pm 3$ responses for the EW guiding signals are different from zero, while nothing is transmitted for other m . For the NS guiding signals, only $m = \pm 2, 0$ are transmitted. The visibilities in the power spectrum for EW and NS guiding signals are identical.

⁶ sum over the transmitted modes

Appendix D: Observed visibility ratios

Table D.1. Observed and theoretical log of visibility ratios for FD signals, obtained by minimizing the difference with the observed ratios; the adjusted outer science pixel radius is 0.941 ± 0.08 derived by minimizing visibility differences

Ratio	theor.	obs.	diff.
$l = 1/0$	+0.488	$+0.498 \pm 0.030$	$+0.010 \pm 0.020$
$l = 2/0$	-0.446	-0.444 ± 0.009	$+0.002 \pm 0.009$
$l = 3/1$	-3.912	-3.276 ± 0.028	$+0.636 \pm 0.020$

Table D.2. Observed and theoretical log of visibility ratios for resolved signals, obtained using the adjusted outer science pixel radius of 0.941 ± 0.08 derived by minimizing the visibility differences in Table D.1

Degree	Ratio	theor.	obs.	diff.
1	$m = 0/1$	-0.701	-0.684 ± 0.078	$+0.017 \pm 0.078$
2	$m = 0/2$	-0.674	-0.464 ± 0.046	$+0.210 \pm 0.046$
3	$m = 1/2$	-0.348	-0.286 ± 0.038	$+0.062 \pm 0.038$
3	$m = 0/3$	-0.698	-0.677 ± 0.066	$+0.021 \pm 0.066$
3	$m = 1/3$	-0.448	-0.489 ± 0.052	-0.041 ± 0.052
3	$m = 2/3$	-0.274	-0.341 ± 0.034	-0.067 ± 0.034
1	$m = 1 / \text{FD}$	-0.068	-0.266 ± 0.020	-0.198 ± 0.020
2	$m = 2 / \text{FD}$	+0.821	0.653 ± 0.019	-0.180 ± 0.019

Table D.3. Observed and theoretical log of visibility ratios for the EW and NS difference signals, obtained using the adjusted outer science pixel radius of 0.941 ± 0.08 derived by minimizing the visibility differences in Table D.1.

Ratio	theor.	obs.	diff.
$l = 2/1$ (EW)	+0.762	$+0.717 \pm 0.030$	-0.045 ± 0.020
$l = 3/1$ (EW)	+0.216	$+0.340 \pm 0.008$	$+0.124 \pm 0.008$
$l = 2/1$ (NS)	+0.730	$+0.716 \pm 0.020$	-0.014 ± 0.020
$l = 3/1$ (NS)	+0.318	$+0.234 \pm 0.008$	-0.084 ± 0.007
$l = 1$ EW / FD	-0.652	-0.685 ± 0.061	-0.023 ± 0.060
$l = 2$ EW / FD	+1.059	$+0.982 \pm 0.017$	-0.077 ± 0.060
$l = 1$ NS / FD	-0.770	-0.707 ± 0.063	$+0.063 \pm 0.060$
$l = 2$ NS / FD	+0.909	$+0.934 \pm 0.022$	$+0.025 \pm 0.060$

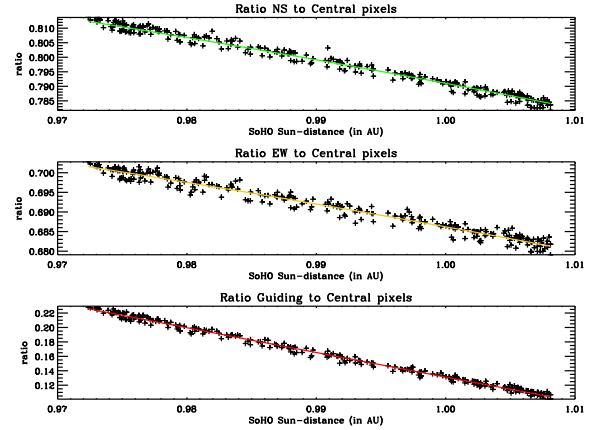


Fig. D.1. Ratio of pixel signals as a function of the SoHO Sun-distance and the associated fit: (top) ratio of the north-south pixels to the central pixels (crosses), fit (green line); (middle) ratio of the east-west pixels to the central pixels (crosses), fit (orange line); (bottom) ratio of the Guiding pixels to the central pixels (crosses), fit (red line).

Table D.4. Observed and theoretical log of visibility ratios for the EW and NS HV signals and the EW and NS guiding pixels, obtained using the adjusted outer science pixel radius of 0.941 ± 0.08 derived by minimizing visibility the differences in Table D.1

Ratio	theor.	obs.	diff.
$l = 2/1$ (EW _{HV})	-1.570	0.848 ± 0.042	$+2.418 \pm 0.042$
$l = 3/1$ (EW _{HV})	-0.414	0.455 ± 0.028	$+0.869 \pm 0.028$
$l = 2/1$ (NS _{HV})	-1.570	0.762 ± 0.047	$+2.332 \pm 0.047$
$l = 3/1$ (NS _{HV})	-0.414	0.539 ± 0.036	$+0.953 \pm 0.036$
$l = 1$ (EW / NS) _{HV}	0.000	0.349 ± 0.067	$+0.349 \pm 0.067$
$l = 2$ (EW / NS) _{HV}	0.000	0.411 ± 0.039	$+0.411 \pm 0.039$

Table D.5. Observed and theoretical log of visibility ratios for the EW and NS HV signals and the EW and NS guiding pixels, obtained using the adjusted outer science pixel radius of 0.941 ± 0.08 derived by minimizing the visibility differences in Table D.1. The visibility ratios are only an estimate since there is only a one-year time series for the guiding pixels.

Ratio	theor.	obs.	diff.
$l = 1$ EW HV/gui.	+2.91	≈ 0.22	≈ -2.70
$l = 1$ NS HV/gui.	+2.91	≈ 1.61	≈ -1.30
$l = 2$ EW HV/gui.	-1.56	≈ 0.07	$\approx +1.63$
$l = 2$ NS HV/gui.	-1.56	≈ 0.91	$\approx +2.57$

Appendix E: Frequencies

Table E.1. Mode frequencies in μHz from global fitting of the 29 years of FD data. [†]These frequencies were obtained with a local fit of the FD data.

n	$l = 0$	$l = 1$	$l = 2$	$l = 3$
11	$1686.599 \pm 0.011^{\dagger}$	-	-	-
12	$1822.300 \pm 0.044^{\dagger}$	1885.134 ± 0.023	1945.860 ± 0.057	
13	1957.538 ± 0.033	2020.900 ± 0.030	2082.156 ± 0.036	
14	2093.543 ± 0.019	2156.918 ± 0.025	2217.730 ± 0.048	
15	2228.846 ± 0.021	2292.082 ± 0.015	2352.384 ± 0.042	
16	2362.889 ± 0.020	2425.705 ± 0.013	2486.010 ± 0.030	
17	2496.286 ± 0.017	2559.291 ± 0.015	2619.766 ± 0.020	
18	2629.754 ± 0.010	2693.494 ± 0.009	2754.594 ± 0.015	2811.334 ± 0.079
19	2764.271 ± 0.011	2828.281 ± 0.012	2889.676 ± 0.015	2946.893 ± 0.048
20	2899.098 ± 0.012	2963.441 ± 0.012	3024.819 ± 0.013	3082.315 ± 0.032
21	3033.864 ± 0.012	3098.310 ± 0.011	3159.989 ± 0.016	3217.731 ± 0.038
22	3168.738 ± 0.013	3233.317 ± 0.013	3295.155 ± 0.020	3353.318 ± 0.067
23	3303.663 ± 0.016	3368.741 ± 0.016	3430.861 ± 0.028	3489.452 ± 0.104
24	3439.152 ± 0.023	3504.460 ± 0.023	3566.921 ± 0.043	3625.931 ± 0.179
25	3575.007 ± 0.028	3640.773 ± 0.032	3703.428 ± 0.067	3762.616 ± 0.360
26	3711.196 ± 0.051	3777.291 ± 0.044	3840.297 ± 0.096	3900.347 ± 0.595
27	3847.985 ± 0.057	3914.350 ± 0.064	3977.802 ± 0.189	4043.565 ± 0.016
28	3985.001 ± 0.122	4051.804 ± 0.084	4115.178 ± 0.199	4197.790 ± 0.893
29	4122.931 ± 0.147	4189.064 ± 0.107	4262.748 ± 0.087	4339.006 ± 0.900
30	4255.467 ± 0.075	4327.551 ± 0.118	4391.455 ± 0.155	4473.272 ± 1.319
31	4399.915 ± 0.192	4466.338 ± 0.175	4530.130 ± 0.178	
32	4538.289 ± 0.140	4605.468 ± 0.237	4683.535 ± 0.417	
33	4672.324 ± 0.168	4745.060 ± 0.261	-	

Table E.2. Mode frequencies from local fitting of the 29 years of resolved data with the collapsogram technique. [†]These frequencies were also obtained with the global fit.

n	$l = 0$	$l = 1$	$l = 2$	$l = 3$
9	-	-	-	1591.559 ± 0.012
10	-	-	1674.546 ± 0.015	1729.144 ± 0.021
11	-	1749.334 ± 0.028	1810.301 ± 0.016	-
12	-	$1885.145 \pm 0.020^{\dagger}$	$1945.886 \pm 0.016^{\dagger}$	-

Appendix F: Linewidths and mode heights

Table F.1. Log of mode linewidths (in μHz) and mode height (in $\text{ppm}^2/\mu\text{Hz}$) from global fitting of the 29 years of FD data for the $l = 0$ modes. [†]These linewidths are derived from the collapsogram analysis of the $l=2$ modes.

n	frequency (μHz)	log(linewidth)	log(height)
11 [†]	1674.55	-1.688 ± 0.333	-
12 [†]	1810.30	-1.181 ± 0.191	-
13	1957.54	-1.666 ± 0.084	-0.785 ± 0.097
14	2093.54	-1.017 ± 0.046	-0.820 ± 0.048
15	2228.85	-0.995 ± 0.032	-0.340 ± 0.032
16	2362.89	-0.641 ± 0.025	-0.149 ± 0.023
17	2496.29	-0.228 ± 0.020	-0.022 ± 0.017
18	2629.75	$+0.309 \pm 0.026$	-0.085 ± 0.019
19	2764.27	$+0.711 \pm 0.015$	-0.052 ± 0.010
20	2899.10	$+1.079 \pm 0.012$	-0.096 ± 0.008
21	3033.86	$+1.230 \pm 0.013$	-0.015 ± 0.008
22	3168.74	$+0.993 \pm 0.010$	$+0.227 \pm 0.007$
23	3303.66	$+0.512 \pm 0.011$	$+0.508 \pm 0.007$
24	3439.15	-0.281 ± 0.011	$+0.936 \pm 0.009$
25	3575.01	-1.055 ± 0.016	$+1.306 \pm 0.012$
26	3711.20	-1.782 ± 0.009	$+1.661 \pm 0.009$
27	3847.98	-2.493 ± 0.015	$+1.974 \pm 0.012$
28	3985.00	-3.087 ± 0.013	$+2.241 \pm 0.013$
29	4122.93	-3.625 ± 0.016	$+2.408 \pm 0.014$
30	4255.47	-4.121 ± 0.017	$+2.613 \pm 0.014$
31	4399.91	-4.509 ± 0.026	$+2.639 \pm 0.028$
32	4538.29	-5.063 ± 0.025	$+2.668 \pm 0.022$
33	4672.32	-5.260 ± 0.024	$+2.836 \pm 0.023$

Table F.2. Log of mode linewidths (in μHz) and mode height (in $\text{ppm}^2/\mu\text{Hz}$) from global fitting of the 29 years of FD data for the $l = 1$ modes. [†]These linewidths are derived from the collapsogram analysis of the $l=3$ modes.

n	frequency (μHz)	log(linewidth)	log(height)
10 [†]	1591.56	2.492 ± 0.566	-
11 [†]	1729.14	-1.565 ± 0.246	-
12	1885.13	-1.328 ± 0.132	-1.041 ± 0.148
13	2020.90	-0.811 ± 0.070	-0.477 ± 0.074
14	2156.92	-0.572 ± 0.040	-0.494 ± 0.041
15	2292.08	-0.149 ± 0.044	-0.413 ± 0.038
16	2425.70	$+0.157 \pm 0.041$	-0.137 ± 0.033
17	2559.29	$+0.521 \pm 0.018$	-0.056 ± 0.013
18	2693.49	$+0.935 \pm 0.020$	-0.056 ± 0.013
19	2828.28	$+1.319 \pm 0.014$	-0.065 ± 0.009
20	2963.44	$+1.573 \pm 0.014$	-0.020 ± 0.009
21	3098.31	$+1.579 \pm 0.013$	$+0.105 \pm 0.008$
22	3233.32	$+1.272 \pm 0.015$	$+0.331 \pm 0.009$
23	3368.74	$+0.674 \pm 0.012$	$+0.654 \pm 0.008$
24	3504.46	-0.086 ± 0.010	$+1.038 \pm 0.007$
25	3640.77	-0.882 ± 0.010	$+1.418 \pm 0.007$
26	3777.29	-1.597 ± 0.010	$+1.732 \pm 0.008$
27	3914.35	-2.285 ± 0.011	$+2.054 \pm 0.010$
28	4051.80	-2.854 ± 0.018	$+2.286 \pm 0.016$
29	4189.06	-3.439 ± 0.017	$+2.506 \pm 0.014$
30	4327.55	-3.895 ± 0.020	$+2.623 \pm 0.019$
31	4466.34	-4.391 ± 0.028	$+2.812 \pm 0.030$
32	4605.47	-4.764 ± 0.029	$+2.910 \pm 0.034$
33	4745.06	-5.169 ± 0.035	$+2.876 \pm 0.052$